Published in final edited form as:

Cell. 2019 September 19; 179(1): 132–146.e14. doi:10.1016/j.cell.2019.08.025.

The Golgi Outpost Protein TPPP Nucleates Microtubules and is Critical for Myelination

Meng-meng Fu[1,8,*], **Thomas S. McAlear**[2], **Huy Nguyen**[3], **Juan A. Oses-Prieto**[4], **Alex Valenzuela**[1], **Rebecca D. Shi**[5], **John J. Perrino**[6], **Ting-Ting Huang**[3,7], **Alma L. Burlingame**[4], **Susanne Bechstedt**[2,*], **Ben A. Barres**[1]

[1] Department of Neurobiology, Stanford University School of Medicine, Stanford, CA 94305, USA

[2] Department of Anatomy and Cell Biology, McGill University, Montreal, Quebec, H3A 0C7, Canada

[3] Department of Neurology and Neurological Sciences, Stanford University School of Medicine, Stanford, CA 94305, USA

[4] Department of Pharmaceutical Chemistry, University of California, San Francisco, San Francisco, CA 94158, USA

[5] Neuroscience Graduate Program, Stanford University School of Medicine, Stanford, CA 94305, USA

[6] Cell Science Imaging Facility, Stanford University School of Medicine, Stanford, CA 94305, USA

[7] Geriatric Research, Education, and Care Center, VA Palo Alto Health Care System, Palo Alto, CA 94304, CA, USA

[8] Lead Contact

SUMMARY

Oligodendrocytes extend elaborate microtubule arbors that contact up to 50 axon segments per cell, then spiral around myelin sheaths, penetrating from outer to inner layers. However, how they establish this complex cytoarchitecture is unclear. Here, we show that oligodendrocytes contain Golgi outposts, an organelle that can function as an acentrosomal microtubule organizing center (MTOC). We identify a specific marker for Golgi outposts – TPPP (tubulin polymerization promoting protein), which we use to purify this organelle and characterize its proteome. In in vitro cell-free assays, recombinant TPPP nucleates microtubules. Primary oligodendrocytes from TPPP knockout (KO) mice have aberrant microtubule branching, mixed microtubule polarity, and shorter myelin sheaths when cultured on 3-dimensional (3D) microfibers. TPPP KO mice exhibit hypomyelination with shorter, thinner myelin sheaths and motor coordination deficits. Together,

---

[*] Co-correspondence: mengmengfu@gmail.com (M.-m.F.), susanne.bechstedt@mcgill.ca (S.B.).

AUTHOR CONTRIBUTIONS

Conceptualization, M.-m.F., S.B., B.A.B.; Methodology, M.-m.F., S.B., T.S.M., A.L.B., J.A.O.-P., H.N., J.J.P.; Investigation and Formal Analysis, M.-m.F., A.V., T.S.M., S.B., H.N., J.A.O.-P., J.J.P., R.D.S.; Writing – Original Draft, M.-m.F., S.B.; Writing – Review & Editing, T.S.M., J.A.O.-P., A.V., R.D.S., J.J.P.; Supervision and Funding Acquisition, B.A.B., M.-m.F., S.B., A.L.B., T.-T.H.

DECLARATION OF INTERESTS

The authors declare no competing interests.

our data demonstrate that microtubule nucleation outside the cell body at Golgi outposts by TPPP is critical for elongation of the myelin sheath.

INTRODUCTION

The microtubule architecture of the oligodendrocyte is one of the most intriguing of any cell type. Each oligodendrocyte in the central nervous system can produce up to 50 myelin sheaths (Chong et al., 2012; Hughes et al., 2018), which insulate neuronal axons to facilitate fast action potential propagation. In contrast, Schwann cells of the peripheral nervous system only produce one myelin sheath per cell. The oligodendrocyte accomplishes this extraordinary cellular feat by producing 2 functional classes of microtubules – proximal microtubules that extend toward the axon (radial microtubules) and distal microtubules that spiral around the myelin sheath (lamellar microtubules). Lamellar microtubules are enclosed inside cytoplasmic channels that tunnel inside the myelin sheath, from the outermost to innermost layer, and can facilitate fast vesicular transport (Snaidero et al., 2014).

Microtubules facilitate transport in oligodendrocytes and may play a crucial role in disease. Oligodendrocytes rely on transport of endosomes (Trajkovic et al., 2006) and mRNA (Carson et al., 1997; Herbert et al., 2017) for delivery and translation of myelin proteins, and of exosomes for communication with neurons (Fruhbeis et al., 2013). Recent studies have uncovered mutations in the β-tubulin gene *Tubb4a* that are causative of debilitating white matter disease in children and hypomyelination in the classic *taiep* rat model (Duncan et al., 2017; Simons et al., 2013). Despite these advances, the mechanisms underlying microtubule organization in oligodendrocytes remain enigmatic.

Classically, new microtubules form at the perinuclear centrosome, a microtubule-organizing center (MTOC) that relies on γ-tubulin to nucleate microtubules (Stearns et al., 1991). In recent years, additional MTOCs have also been identified, including Golgi stacks in the cell body (Chabin-Brion et al., 2001; Efimov et al., 2007), virus assembly compartments derived from Golgi (Procter et al., 2018), nuclear envelopes in muscle cells (Gimpel et al., 2017), and interphase bridges in early embryos (Zenker et al., 2017).

Among specialized cells with ramified cytoarchitecture, neurons have been the focus of many studies on microtubule organization. Mammalian neurons have 2 types of processes – typically one long axon with uniform microtubule polarity (plus-ends growing away from the cell body) and many branched dendrites with mixed microtubule polarity (Baas et al., 1988; Burton and Paige, 1981; Stepanova et al., 2003; Yau et al., 2016). Two mechanisms have been proposed to explain how neurons build these processes – microtubule transport and local nucleation. First, microtubules transported from the cell body (Wang and Brown, 2002) can be severed by katanin or spastin and act as seeds for polymerization. Second, acentrosomal MTOCs outside of the cell body may nucleate the formation of new microtubules. In axons, cultured rat neurons whose centrosomes were laser ablated continue to extend axons many days later (Stiess et al., 2010). In dendrites, satellite organelles called Golgi outposts can act as sites of acentrosomal nucleation in *Drosophila* neurons (Ori-McKenney et al., 2012). However, this finding has been challenged in experiments using

Golgi-kinesin fusion proteins to recruit Golgi outposts out of the dendrite (Nguyen et al., 2014).

Interestingly, Golgi outposts have also been found in gastric parietal cells (Gunn et al., 2011) and in muscle cells, where they are positioned at the intersections of microtubules that form a grid-like lattice (Oddoux et al., 2013). However, acentrosomal microtubule nucleation has yet to be described in oligodendrocytes or other glial cells. In addition, because Golgi in the cell body can also function as a site for microtubule nucleation (Chabin-Brion et al., 2001; Efimov et al., 2007), a challenge to studying Golgi outposts is the lack of an organelle-specific marker that does not recognize cell body Golgi.

Here, we show that oligodendrocytes contain Golgi outposts and identify a new marker for Golgi outposts – TPPP (tubulin polymerization promoting protein). This discovery allowed us to purify Golgi outposts from brain and characterize the proteome of this organelle for the first time. We demonstrate using biophysical assays that TPPP nucleates microtubules. In vitro, cultured TPPP KO oligodendrocytes surprisingly have more proximal microtubules and no defects in number of myelin sheaths formed. However, oligodendrocytes cultured on 3D microfibers contain Golgi outposts along nascent myelin sheaths and TPPP KO cells have shorter myelin sheaths. In vivo, TPPP KO mice are hypomyelinated with shorter and thinner sheaths and have motor coordination defects. Together, our data demonstrate that TPPP on Golgi outposts are important for local microtubule nucleation and myelin sheath elongation.

RESULTS

Oligodendrocytes Have Uniform Microtubule Polarity

Classic electron microscopy (EM) experiments using the “hooking” technique in oligodendrocytes demonstrated that ~80% of microtubules in large diameter processes have plus-end out orientation (Lunn et al., 1997). In order to validate this using live-cell microscopy, we expressed the plus-end microtubule-binding protein EB3-EGFP in primary rat oligodendrocytes purified via the immunopanning method. When differentiated in culture, oligodendrocytes extend many microtubules that become increasingly complex in arborization with increasing days in vitro (DIV; Figure 1A).

Kymograph analysis of EB3 dynamics demonstrates that DIV 1–5 oligodendrocytes have uniform polarity with ~85–92% of microtubules growing away from the cell body (Figure 1B, 1C, and Video 1). Interestingly, EB3 speeds varied, with the lowest speed ~0.09 μm/s at DIV1 and the fastest speed ~0.16 μm/s at DIV2 (Figure 1D), indicating that polymerization is faster at certain developmental periods. The average length of microtubule growth phases did not change from DIV1–5 (Figure 1E). In addition, proliferating oligodendrocyte precursor cells (OPCs), which have bipolar processes, also have uniform microtubule polarity with ~97% plus-ends out (Figures S1A–S1C).

Oligodendrocytes Contain Golgi Outposts

Golgi outposts have been found in both fly (Zhou et al., 2014) and mammalian neuronal dendrites (Horton et al., 2005; Quassollo et al., 2015) using the *cis* Golgi marker GM130. In order to determine whether primary rat oligodendrocytes also contain Golgi outposts, we immunostained them and observed GM130-positive (GM130+) puncta along microtubule processes (Figure 1F), with 34.1 ± 8.9% located at branch points. Golgi outposts are distributed along primary, secondary and tertiary, but not quaternary, processes (Figure 1G) and at various distances away from the cell center with a non-normal or random distribution (Figure 1H).

Over 2 decades ago, EM of cultured oligodendrocyte revealed “outstations of Golgi complex” along cell processes. These organelles were in close proximity to microtubules and ~1–3 μm in length (de Vries et al., 1993), much smaller than Golgi stacks in the cell body. Thus, we asked whether Golgi outposts could also be observed *in vivo*. Transmission EM (TEM) images of mouse spinal cords at P14 after initiation of myelination show Golgi outposts in the proximal branches of oligodendrocytes (Figure 1I). These structures are ~1–2 μm in length and contain multiple stacks with small associated vesicular structures, which suggests that *cis*, *medial*, and *trans* Golgi can be found intact in a single Golgi outpost. We also observed Golgi outposts far from nuclei in thin processes (Figure S1D), but it is unclear if they are from oligodendrocytes.

Functionally, in order to determine whether Golgi outposts could be a source for growing microtubules, we performed dual-color live-cell imaging using the *medial* Golgi marker mannosidase II (ManII) and EB3. Indeed, kymographs demonstrate that the 32–41% of ManII-positive (ManII+) puncta colocalize with the initiation of EB3 events during 3-minute imaging periods (Figures S2A–S2C), indicating that microtubule plus-ends at the start of their growth phase are located in the vicinity of Golgi outposts. The observed rate of EB3s arising from ManII+ puncta was >3 times higher than the probability based on chance (Figure S2D). Binning by speed indicates that ManII+ puncta that give rise to EB3 events are relatively stationary with mean speed of 0.013 ± 0.006 μm/s (Figure S2E). Thus, while a subpopulation of stationary Golgi outposts can give rise to newly growing microtubules, a separate subpopulation of motile Golgi may have other functions, such as secretion and transport (Horton et al., 2005; Ye et al., 2007).

TPPP is a Specific Marker for Golgi Outposts

Since oligodendrocyte processes possess properties found in both mammalian axons (e.g. uniform microtubule polarity) and dendrites (e.g. Golgi outposts), we hypothesized that cell-specific mechanisms may underlie the assembly of this unique microtubule architecture. Thus, we performed a screen for microtubule-associated proteins (MAPs) that are both highly and specifically expressed by oligodendrocytes in a RNA-seq database of immunopanned P5 brain cells (Zhang et al., 2014).

One candidate from this screen was TPPP, a small ~25-kDa MAP, whose mRNA expression is high in oligodendrocytes and very low in neurons, astrocytes, and microglia (Figure 2A). Classic experiments indicate that TPPP protein is absent in the embryonic brain and increases in the postnatal brain around P11 (Takahashi et al., 1993), coincident with the start of myelination. Using a validated anti-TPPP antibody (Figures S4A and S5B), we detected TPPP-positive (TPPP+) puncta along oligodendrocyte processes (Figure 2B). Strikingly, 93% of TPPP+ puncta colocalized with GM130 (Figure 2C). Importantly, no TPPP+ puncta colocalized with GM130+ Golgi stacks in the cell body, indicating that TPPP is a specific marker for Golgi outposts. We also replicated this staining pattern using super-resolution microscopy (Figures 2D and S2F).

Functionally, to determine whether TPPP+ Golgi outposts can give rise to microtubules, we first looked for endogenous colocalization of TPPP and EB1. Indeed, 34% of TPPP+ puncta colocalize with EB1 (Figures 2E and 2F), indicating that at the time of fixation, a high percent of TPPP+ puncta are in close proximity to growing microtubules. Next, we performed dual-color live-cell imaging to show that EB3-labeled growing microtubules can emanate from TPPP-EGFP puncta (Figure 2G). The observed rate of EBs arising from TPPP puncta was >5 times higher than the probability based on chance (Figure 2H). We also used the binomial distribution to calculate the mean probability of these outcomes (0.08). TPPP-GFP puncta are relatively stationary with speed of 0.009 ± 0.002 μm/s, consistent with the observation that stationary ManII+ Golgi preferentially give rise to EBs (Figure S2E).

Purification and Mass Spectrometry (MS) of Golgi Outposts

In order to further validate TPPP as a Golgi outpost marker, we biochemically purified Golgi outposts by adapting an established sucrose gradient ultracentrifugation protocol for Golgi purification (Wang et al., 2006) to use 8 P10 neonatal rat brains (Figure 3A); we chose this age to coincide with the start of myelination. To confirm purification of Golgi, we performed Western blots that showed enrichment of both GM130 and TPPP in the resulting Golgi fraction (Figure 3B). We expected this purified Golgi fraction to contain both Golgi stacks from the cell body as well as Golgi outposts. Thus, we further isolated it via immuno-EM and immunoprecipitation (IP).

To visualize purified Golgi outposts, we performed immuno-EM using gold beads labeled with anti-TPPP antibody. Bead-associated Golgis are membranous structures with diameters ~1–2 μm (Figure 3C), similar in size to Golgi outposts in spinal cord EMs (Figure 1I). Importantly, ~69% of bead-associated Golgi co-purified with microtubules (n = 13 Golgis; 3.67 ± 1.09 microtubules per microtubule-associated Golgi). This further supports that TPPP + Golgi outposts can give rise to microtubules.

In parallel, we IP'ed purified Golgi fractions using magnetic beads conjugated to anti-TPPP antibody. In order to eliminate eluted proteins that nonspecifically adsorb to beads, we used anti-GFP antibody as a negative control. Western blots confirm that TPPP is present in the anti-TPPP eluate but absent in the anti-GFP eluate (Figure 3D). Three IP samples were analyzed by MS – the input (purified Golgi), the anti-GFP eluate, and the anti-TPPP eluate. We identified 118 proteins that specifically elute with anti-TPPP antibody and are enriched relative to the Golgi input (Figure 3E, Table S1). This proteome represents the subpopulation of TPPP+ Golgi outposts in the brain. Thus, the ~24% of GM130+ puncta in oligodendrocytes that are TPPP-negative (Figure 2C) would not be represented in this proteome. Though we looked for hits of γ-tubulin, none were detected in the anti-TPPP eluate and we failed to detect colocalization by staining with multiple antibodies (Figure S3).

Many top hits are transmembrane proteins, which also confirms that our IPs successfully captured membranous organelles. Unexpectedly, many top hits are signaling proteins that may be trafficked between the Golgi outpost and the plasma membrane. The top hit was Golgi apparatus protein 1, a *medial* Golgi protein implicated in trafficking of FGF receptors (Kohl et al., 2000; Zuber et al., 1997), which affect myelin thickness (Furusho et al., 2012). One well-characterized hit, LDL receptor related protein 1 (LRP1), was recently demonstrated to be crucial for myelination *in vivo* (Lin et al., 2017). Tm9sf2, which belongs to a family of nonaspanins or proteins with 9 transmembrane domains, is involved in trafficking of innate immunity receptors in *Drosophila* (Perrin et al., 2015). A genetic screen recently identified that the *FAM234B* gene is mutated in human patients with intellectual disability (Reuter et al., 2017). Some hits, such as Protein 9330182L06Rik, have yet to be characterized. We validate the hit MYO18A, an unconventional myosin that colocalizes with some GM130+ Golgi outposts (Figure 3F). In HEK293 cells, MYO18A mediates Golgi dispersion following DNA damage through its interaction with the Golgi protein GOLPH3 (Farber-Katz et al., 2014).

TPPP Nucleates Microtubules

In order to understand the molecular function of TPPP, we purified TPPP protein (Figure 4A) and turned to biophysical assays. Previously, addition of TPPP led to increased microtubule density in bulk spectrophotometer assays and was interpreted to mean an increase in polymerization rate (Tirian et al., 2003). However, this approach cannot distinguish between polymerization, stabilization, or nucleation. Thus, we added TPPP in an *in vitro* microtubule dynamics assay and measured growth rate using a total internal reflection fluorescence (TIRF) microscope. We found that TPPP addition had little effect on the growth rate (Figure 4B and 4C).

Unlike other MAPs that localize to microtubule lattices, TPPP in oligodendrocytes localizes to Golgi outposts, which have been shown to act as sites of local microtubule nucleation in *Drosophila* (Ori-McKenney et al., 2012). We therefore asked if TPPP can nucleate microtubules from the surface of a membrane-bound organelle like the Golgi outpost. To reconstitute this cellular geometry, we bound purified TPPP to Ni-NTA beads. In the control condition with no TPPP, tubulin is not recruited to beads and no microtubules form (Figure 4D). When TPPP was loaded onto beads in the absence of GTP, tubulin was recruited to beads (Figure 4E). When GTP was added, TPPP-loaded beads nucleated microtubules rapidly, forming microtubules 5–10 μm long within 3 min (Figure 4F and Video 2). This effect was specific, as other MAPs like EB3 did not nucleate microtubules (Figure S4A). In oligodendrocyte lysates, we also found that TPPP-EGFP puncta similarly recruited tubulin in the absence of GTP (Figure S4B).

TPPP KO Oligodendrocytes Have Microtubule Organization Defects

In *Drosophila* mutants that cannot nucleate microtubules at Golgi outposts, neurons that lack centrosomes have fewer dendritic branches (Ori-McKenney et al., 2012). Because oligodendrocytes have centrosomes (Figures S3B and S3C), a decrease in microtubule processes in TPPP KO oligodendrocytes would indicate that centrosome-derived microtubules cannot compensate for loss of Golgi outpost nucleation. When we cultured oligodendrocytes from a global TPPP KO mouse (validated with antibody staining, Figures S6A and S6B), we surprisingly observed an increased number of proximal microtubule processes (<15 µm from the cell body) by Sholl analysis of the number of process intersections at discrete distances away from the cell body (Figures 5A–5C). Thus, oligodendrocytes can compensate for TPPP loss, perhaps with centrosome-derived microtubules, which in neurons can be transported from the cell body to axons (Wang and Brown, 2002). To test whether this effect is specific to different brain regions, we knocked down TPPP using siRNA and found that rat oligodendrocytes cultured from both spinal cord and cortex display this defect (Figure S5).

In vitro studies and overexpression in HeLa cells have proposed a role for TPPP as a microtubule bundler (Vincze et al., 2006). We hypothesized that global loss of bundling would result in loosely organized, thicker primary branches. In contrast, TPPP KO oligodendrocytes have thinner primary processes (Figure 5D). To test whether TPPP or associated MAPs may have a parallel bundling or microtubule alignment role locally at Golgi ouposts, we performed EB3 live-cell imaging. TPPP KO oligodendrocytes no longer display uniform microtubule polarity, with 53.1 ± 2.0% of EB3s directed back toward the cell body (Figures 5E and 5F, Video 3). Neither microtubule growth length nor speed changed (Figures 5G and 5H). Because EB3 speed is a live-cell reporter of microtubule growth rate, this demonstrates that TPPP does not promote enhanced microtubule growth speed in oligodendrocytes, consistent with our in vitro results (Figures 4B and 4C). Instead, we observe a decrease in anterograde EB3s in TPPP KO distal processes (Figure 5I), indicative of decreased microtubule nucleation. Thus, we clarify that the name TPPP (tubulin polymerization promoting protein) appropriately refers to its propensity to promote microtubule nucleation, not growth. These data support a model where TPPP on Golgi outposts is important for both uniform polarized growth of distal microtubules as well as directing the branching of proximal processes (Figure 5J).

Consistent with this model, we find that TPPP KO oligodendrocytes upregulate the number of Golgi outposts, perhaps to compensate for decreased microtubule growth in distal processes, but the ultrastructure of these microtubules are morphologically normal (Figures 5K and 5L). In addition, to test whether TPPP KO oligodendrocytes have cargo transport defects, we generated single molecule fluorescent in situ hybridization (smFISH) probes against mouse *Mbp* (myelin basic protein) mRNA. In DIV4 TPPP KO cells, *Mbp* mRNAs are distributed along microtubules, but are larger (Figures 5M–5O), perhaps indicative of aggregation. Since MBP protein translation begins around DIV4, we also observed a trend toward decreased MBP protein intensity in TPPP KO cells (n.s., p = 0.095, Figures S5F and S5G).

TPPP KO Oligodendrocytes Have Shorter Myelin Sheaths

Mature oligodendrocytes have complex 3D morphology; therefore, we asked whether TPPP also has a role in forming lamellar microtubules inside the myelin sheaths. We addressed this using 2 techniques – in vitro in DIV14 oligodendrocytes cultured on 3D microfibers that mimic axons and in vivo in sparsely myelinated regions of P14 mouse cortex (Figures 6A and S6A). We hypothesized that: 1) if radial microtubules were impeded in contacting axons, then we would find fewer myelin sheaths, and that 2) if lamellar microtubules were defective, then we would find shorter and thinner myelin sheaths.

In vitro, oligodendrocytes cultured on 3D microfibers contain Golgi outposts along nascent myelin sheaths that colocalize with lamellar microtubules (Figures 6B and S6B). Compared to wildtype (WT) cells, TPPP KO oligodendrocytes stained against MBP had no difference in the number of myelin sheaths per cell (Figures 6C and 6D), but their sheaths were significantly shorter, about half the length of WT ones (Figures 6E and 6F). The length of lamellar microtubules along the myelin sheath similarly decreased (Figure 6G), consistent with decreased EB3 flux in distal processes (Figure 5I). At higher magnification, each WT myelin sheath generally associates with 1 lamellar microtubule, but TPPP KO lamellar microtubules are highly disorganized and appear either to have multiple microtubules per sheath and/or to spiral many times around the sheath with high degrees of curvature (Figure S6C). In addition, MBP along WT sheaths appears smoother, but MBP along TPPP KO sheaths appears splotchy and punctate with occasional bulbous large hyperintensities reminiscent of myelin outfoldings (Figure S6C).

In vivo, we imaged thick sections of P14 cortex on a confocal microscope with 0.2-μm z-stacks. Similar to in vitro results, TPPP KO cells have no difference in number of sheaths per cell, but decreased myelin sheath length (Figures 6H–6K, Videos 4 and 5). By measuring the boundaries of MBP-positive myelin sheaths, we also calculated the combined radius of myelin and axons, which decreased in TPPP KO cells (Figure 6L). Thus, TPPP KO oligodendrocytes have radial microtubules that are not functionally impaired, but shorter lamellar microtubules that result in shorter myelin sheaths.

TPPP is Required for Myelination *in vivo*

To further interrogate the myelin ultrastructure, we performed TEM of adult optic nerves. TPPP KO mice have higher g-ratio (ratio between the axonal and myelin diameters), but no change in axon diameter (Figures 7A–7D); thus, TPPP KO mice have thinner myelin sheaths. We observed no difference in percent of axons myelinated (Figure 7E), consistent with *in vitro* and *in vivo* measurements of number of myelin sheaths per cell (Figures 6D and 6I). Interestingly, TPPP KO axons have a greater percent of area occupied by organelles (Figure 7F). This may be a preceding step to remarkable accumulations of organelles, including mitochondria, multi-vesicular bodies, and autophagosomes, in some TPPP KO axons (Figure 7G). These axonal swellings likely indicate axonal transport dysfunction and degeneration and have also been observed in mouse mutants lacking myelin proteins, including *Cnp* and *Plp* null mice (Edgar et al., 2009; Edgar et al., 2004).

To look at myelination globally across the brain, we stained against MBP and found that adult TPPP KO mice have decreased MBP staining in the cortex, spinal cord, caudate, and hippocampus, and are almost devoid of signal in upper cortical layers and along CA1 and CA3 fiber tracts (Figures 7H and 7I). We did not observe any gross differences in neuronal staining with an anti-neurofilament antibody (Figure S4C). A different TPPP antibody also did not detect TPPP expression in astrocytes or cortical or sensory neurons (Goldbaum et al., 2008). Single-cell RNA-seq databases confirm that TPPP has low expression in adult neurons (Figures S7A and S7B). However, in embryonic neurons, which are at the developmental period of extending microtubule arbors, a subpopulation of CA3 pyramidal neurons do express TPPP (Figure S7C).

Behaviorally, TPPP KO mice displayed breeding and motor coordination defects. The majority of TPPP KO mice have never successfully bred, even when paired with proven breeders. Thus, we maintained our colony using heterozygotes. Compared to WT mice, TPPP KO mice fall off the Rotarod faster during training and about twice as fast on the third testing day (Figure 7J). These behavioral deficits in TPPP KO mice are likely attributed to hypomyelination in multiple brain regions.

DISCUSSION

Here, we showed that TPPP has little effect on microtubule growth rates, but, instead, acts as a powerful nucleator of microtubules. We propose that the propensity of TPPP to nucleate microtubules is harnessed at Golgi outposts and is especially important for elongation of the myelin sheath. In the absence of TPPP, oligodendrocytes compensate by extending more proximal radial microtubules and the number of sheaths generated per cell is unchanged. However, length of lamellar microtubules along the myelin sheath is decreased, resulting in shorter myelin sheaths both in vitro in 3D cultures and in vivo in the cortex.

In many ways, our findings raise more questions than answers. Though we have demonstrated that TPPP is a Golgi outpost marker, it is unclear how it localizes to this membranous organelle with no predicted transmembrane domains. However, dual-color live-cell imaging with ManII and TPPP (Figures 2G, 2H, S3) suggests that TPPP is preferentially recruited to a subpopulation of stationary Golgi outposts. Anchoring of stationary Golgi outposts may be important for two reasons – to counteract the force generated from microtubule polymerization and to regulate branching. Local nucleation sites where nascent microtubules are not aligned with pre-existing microtubules could become sites of new branches (Figure 5J). In neurons, Golgi in the cell body undergo fusion to form nascent Golgi outposts, which are then transported along dendrites (Quassollo et al., 2015). Our MS data may offer some hints as to how Golgi outposts are transported or anchored. MYO18A (Figure 3F and Table 1) is an unconventional myosin that contains a PDZ domain for membrane association and has been proposed to act as an actin-tethering protein (Guzik-Lendrum et al., 2011).

A conundrum raised by our experiments is that TPPP is a symmetric microtubule nucleator in cell-free biophysics assays, but TPPP KO cells have mixed rather than uniform microtubule polarity, indicating that local nucleation off of Golgi outposts is asymmetric. We suggest two mechanisms, which are not mutually exclusive. First, the Golgi outpost, as an asymmetric organelle with *cis*, *medial* and *trans* stacks (Zhou et al., 2014), may adopt a specific spatial orientation inside the oligodendrocyte process that only facilitates microtubule nucleation in one direction, similar to asymmetric nucleation off of Golgi in the cell body (Efimov et al., 2007). Second, TPPP may form a complex with other MAPs that bundle or align nascent microtubules with pre-existing microtubules by restricting the angle of nucleation, similar to augmin in the axon (Petry et al., 2013; Sanchez-Huertas et al., 2016). An important prediction of this model is that removal of bundling/alignment MAPs would no longer restrict the angle of microtubule growth and therefore may facilitate the formation of new branches (Figure 5L).

Our MS data of TPPP-associated Golgi outposts revealed component of the FGF and LRP signaling pathways (Figure 4E); this raises the intriguing possibility that extracellular cues may locally trigger microtubule nucleation at Golgi outposts. Interestingly, FGF receptor KO mice have thinner myelin sheaths with no difference in percent of axons myelinated (Furusho et al., 2012), while LRP1 knockouts have both thinner sheaths and decreased percent of axons myelinated (Lin et al., 2017). This indicates that different signaling pathways may act in spatially and temporally specific ways to regulate distinct functions – contact with axons by radial microtubules versus myelin sheath growth by lamellar microtubules. Functionally, Golgi outpost signaling may affect the geometry of the myelin sheath through 1) regulating the length of lamellar microtubules, and 2) facilitating *Mbp* mRNA transport. Indeed, we previously demonstrated that defects in *Mbp* mRNA transport can lead to impaired MBP protein translation (Herbert et al., 2017). In other words, microtubule track defects affect the efficiency of mRNA cargo transport, which can subsequently impair MBP translation. Together, these functions are consistent with the defects in TPPP KO myelin sheaths, which are shorter and thinner.

Cues that control myelin sheath formation may be important not only for development, but also for myelin maintenance and plasticity in adult animals. As oligodendrocytes develop *in vivo*, their branches are highly dynamic prior to formation of myelin sheaths (Hughes et al., 2018). Recent experiments in zebrafish demonstrated that synaptic vesicle release can modulate myelination (Koudelka et al., 2016) and that local calcium signals within individual nascent myelin sheaths correlate with whether sheaths retract or elongate (Baraban et al., 2018). In adult mice responding to motor learning (Gibson et al., 2014) or social and environmental changes (Liu et al., 2012), average myelin thickness can change. Thus, local differences in extracellular cues may trigger subcellular responses at the level of radial microtubules (e.g. to form new branches, stabilize pre-existing ones, or retract pre-existing branches) and lamellar microtubules (e.g. to lengthen or thicken the myelin sheath).

During aging, TPPP protein levels progressively increase in rat brains with peak expression at 2 years of age (Takahashi et al., 1993). However, it is unclear if this represents an increased demand for TPPP in the aging brain or aberrant accumulation. Indeed, histology studies have observed TPPP aggregates in Alzheimer’s disease (Frykman et al., 2012) and α-synucleinopathies, including multiple system atrophy (Song et al., 2007), Parkinson’s disease (Kovacs et al., 2004), and Lewy body dementia (Lindersson et al., 2005). In contrast, in multiple sclerosis, TPPP is expressed in remyelinating lesions and increased TPPP levels correlated with shorter disease durations (Hoftberger et al., 2010), indicating a role for TPPP in myelin repair.

A thorough understanding of the helpful versus harmful role of TPPP in aging and diseased brains may require further investigation of TPPP’s role in heterogeneous oligodendrocytes. The original classification by Rio-Hortega of silver-stained oligodendrocytes divided cells into Type I or II cells that form many sheaths around small axons versus Type III or IV that form fewer sheaths around large-caliber axons. More recent publications have shown that the number and lengths of myelin sheaths produced by individual cells greatly vary across different regions of the brain (Chong et al., 2012). However, when cultured on 3D microfibers, sheath length is intrinsic to the regional origin of oligodendrocytes (Bechler et al., 2015). Thus, brain regions with oligodendrocytes with longer myelin sheaths may be more vulnerable to TPPP loss. In our paper, oligodendrocytes imaged in the cortex (Figures 6G–6K) are likely Type I or II. Thus, future experiments should also investigate the 3D morphology of Type III or IV cells in TPPP KOs. Nevertheless, our finding that TPPP KOs have shorter myelin sheaths both in vitro and in vivo is reminiscent of findings in Schwann cells that microtubule defects impair sheath elongation (Court et al., 2004), which suggests that the relationship between lamellar microtubules and sheath length is conserved in both types of myelinating cells.

We began this study by asking basic questions about microtubule polarity in oligodendrocytes. Along the way, we identified TPPP as a Golgi outpost marker and characterized the proteome of this organelle. Studies at the biophysical, cell culture and in vivo levels demonstrate that local microtubule nucleation at Golgi outposts play an important role in building lamellar microtubules and elongating myelin sheaths. We hope our work opens the door to many exciting future questions on the function of Golgi outposts in other specialized cell types, such as muscle and gut cells (Gunn et al., 2011; Oddoux et al., 2013).

STAR METHODS

EXPERIMENTAL MODEL AND SUBJECT DETAILS

Rodent Oligodendrocyte Primary Cell Culture—Oligodendrocyte precursor cells (OPCs) were purified from Sprague-Dawley rat pups (P6–P8) by immunopanning as previously described (Dugas and Emery, 2013). Briefly, cortical tissue was dissociated by papain digestion then filtered through a Nitex mesh to obtain a mixed single-cell suspension. This suspension was incubated in 2 negative-selection plates coated with anti-Ran-2 and anti-GC antibodies, then in a positive-selection plate coated with anti-O4 antibody. Adherent cells were trypsinized and cultured in rat proliferation media containing PDGF and NT-3 or differentiation media containing T3 at 37°C.

Mouse OPCs were isolated from P6–P8 pups by immunopanning as previously described (Emery and Dugas, 2013), using 3 negative-selection plates coated with anti-BSL1 antibody followed by a positive-selection plate coated with anti-PDGFRα antibody. Adherent cells were trypsinized and cultured in mouse differentiation media containing T3 at 37°C. For 3D cultures, 2-μm microfiber inserts for 12-well plates were washed in ethanol, then coated in poly-D-lysine (PDL) hydrobromide, then cultured for 14 days at 37°C.

Mouse Line—All animal procedures were approved by Stanford University’s Administrative Panel on Laboratory Animal Care. TPPP KO mice were recovered from sperm (KOMP stock number VG12652) and bred in the C57BL/6J strain.

For immunohistochemical staining and electron microscopy, 3-months old littermate mice of both genders were anaesthetized with a cocktail of ketamine (100 mg/kg) and xylazine (20 mg/kg) prior to perfusion. For Rotarod assays, 3-months old male littermate mice were used. These ages were selected to represent adult mice. For spinal cord EMs of Golgi outposts, P14 juvenile mice were chosen at a developmental period with robust myelination.

Recombinant Protein Expression in *E. coli*—BL21(DE3) *E. coli* cells containing protein expression vectors were grown to OD 0.6 at 37°C, and expression was induced using 0.5 mM IPTG at 18°C for 16 h.

METHOD DETAILS

Live-Cell Imaging—0.5–1 million immunopanned mouse or rat OPCs were electroporated (Lonza Amaxa Nucleofector, Program O-17) with EB3-EGFP, mCherry-EB3, TPPP-EGFP, or ManII-tdTomato constructs, then plated onto 35-mm No. 1.5 glass-bottom dishes coated with 10 μg/mL PDL hydrobromide. Cells were imaged at the Stanford Cell Sciences Imaging Facility on a spinning disk confocal (Nikon Eclipse-TI inverted microscope with Perfect Focus and Yokogawa spinning disk) with an EMCCD camera (Andor iXon Ultra 897) in an environmental chamber at 37°C with 5% CO2. To decrease phototoxicity, cells were imaged in Hibernate A media and each plate was imaged for total duration of 1 h or less. Images were collected every 3 s for 3–5 min.

Immunocytochemical Staining—Oligodendrocytes were cultured on glass coverslips sonicated for 1 h in ethanol and coated with PDL hydrobromide. Cells were fixed with 4% paraformaldehyde for 10 min, permeabilized with 0.1% Triton X-100 in PBS for 3 min, then blocked with 5% goat or donkey serum with 1% BSA in PBS for 30 min. Primary antibody incubation was performed at 4°C overnight. Secondary antibody incubation was performed at room temperature for 1 h. The following antibodies and dilutions were used: EB1 (1:50), GM130 (1:50), MBP (1:100), MYO18A (1:200), TPPP (1:200), α-tubulin (1:500), α/β-tubulin (1:200), γ-tubulin (DQ-19 1:250, GTU-88 1:500, T3559 1:5000, T5192 1:1000, TU-30 1:50).

For 3D microfiber cultures, oligodendrocytes were fixed and stained on microfibers, then imaged in PBS in a glass-bottom 12-well plate with a 20× objective. Since microfibers are suspended above the glass with a high working distance, suspended microfibers could not be imaged at higher magnification. Thus, microfiber cultures were then squished and mounted with VECTASHIELD on glass coverslips for imaging with a 100× objective.

Samples were imaged on a spinning disk confocal (Nikon Eclipse-TI inverted microscope with Perfect Focus and Yokogawa spinning disk) with an EMCCD camera (Andor iXon Ultra 897) or a Photometrics Prime94B sCMOS camera. Typically Golgi outposts are too small to be resolved by conventional wide-field fluorescence microscopy.

Single Molecule FISH (smFISH)—Custom smFISH probes were designed against mouse *Mbp* mRNA CDS. Cells were stained according to manufacturer's protocol with co-incubation in MBP antibody (1:100). Briefly, cells were fixed in 4% paraformaldehyde, permeabilized in 70% ethanol for 1 hour at 4°C, hybridized with smFISH probes for 4–16 hours at 37°C, washed for 30 minutes at 37°C and then stained with secondary antibody.

Super-resolution microscopy—Oligodendrocytes were plated onto precision No. 1.5H glass coverslips cleaned in 1 M HCl for 30min, then coated with PDL hydrobromide. Cells were immunostained as described, mounted in ProLong Gold overnight, then imaged with 0.2-μm z-stacks at 100× on a 3D-SIM microscope (OMX-BLAZE) with EMCCD camera (Photometrics Evolve 512). Images were reconstructed using SoftWoRx software. All images shown are maximum intensity projections.

Golgi Outpost Purification—We adapted an established protocol for Golgi purification from rat liver (Wang et al., 2006) to use 8 P10 neonatal rat brains as the starting material. Brains were rapidly dissected and Dounce homogenized using the loose pestle. Brain homogenates were spun twice in an ultracentrifuge at 150,000× g for 60 min then at 11,000× g for 30 min. Resulting purified Golgi was then subject to: 1) immuno-EM and 2) immunoprecipitation (IP) against TPPP in order to isolate Golgi outposts for MS analysis.

IP was performed using Protein-G conjugated Dynabeads and anti-GFP or anti-TPPP antibody. Inputs for IPs from each trial were normalized by protein mass determined from BCA assays. Samples for Western blot were eluted following heating at 95°C for 5 min in a denaturing buffer (0.05 M Tris-HCl, 2% SDS, 5% β-mercapthoethanol, 0.12% bromophenol blue, 10% glycerol). Samples for MS were eluted following heating at 95°C for 5 min in a surfactant buffer (0.2% RapiGest, 5 mM DTT, 50 mM ammonium bicarbonate). All replicates were verified by Western blot analysis for efficient Golgi purification and IP.

MS—5mM DTT was added to Golgi input samples, which were then incubated at 60°C for 45 min. Iodoacetamide was added to purified Golgi and eluates to a final concentration of 7.5 mM and incubated for 1 h at room temperature in the dark, followed by an incubation with 1 μg sequencing grade trypsin overnight at 37°C. Digestion was stopped by adding 5% formic acid, and samples were incubated at room temperature for 30 min. The resulting peptides were enriched with OMIX C18 pipette tips and eluted with 50% acetonitrile and 0.1% formic acid. The samples were dried down by SpeedVac and then resuspended in 0.1% formic acid for analysis by LC-MS/MS. Peptides resulting from trypsinization were analyzed either on an QExactive Plus or an Orbitrap Fusion Lumos (Thermo Scientific) connected to a NanoAcquity™ Ultra Performance UPLC system (Waters). A 15-cm EasySpray C18 column was used to resolve peptides (90-min gradient with 0.1% formic acid in water as mobile phase A and 0.1% formic acid in acetonitrile as mobile phase B). MS was operated in data-dependent mode to automatically switch between MS and MS/MS. The top 10 precursor ions with a charge state of 2+ or higher were fragmented by HCD.

Peak lists were generated using PAVA in-house software (Guan et al., 2011). All generated peak lists were searched against the rat subset of the UniProt database (UniprotKB 2017.11.01) using Protein Prospector (Clauser et al., 1999). The database search was performed with the following parameters: a mass tolerance of 20 ppm for precursor masses; 30 ppm for MS/MS, cysteine carbamidomethylation as a fixed modification and methionine oxidation as a variable modification. The enzyme was specified as trypsin with 1 missed cleavage allowed.

Cloning—For bacterial expression, the coding sequence of full-length human TPPP cDNA was PCR amplified using PfuX7 polymerase (Norholm, 2010) and inserted into modified pHAT2 (Peranen et al., 1996) bacterial expression vectors pHAT-HUNS, pHAT-HUScS and pHAT-HUS using the Kunkel method (Kunkel, 1985). The pHAT vectors contain an N-terminal 6-His tag and C-terminal StrepTagII tags. The pHAT-HUNS vector contains mNeonGreen and the pHAT-HUScS vector contains mScarlet between the TPPP coding sequence and the Strep-TagII sequence. Human EB3 was cloned into pHAT-HUScS.

For mammalian expression, TPPP rat cDNA was gene synthesized and the CDS and 3’UTR were inserted into the pEGFP-C1 construct at the following restriction sites: HindIII and SacII, and BsrGI and NotI, respectively.

Protein Expression and Purification—Bacterial pellets were harvested by centrifugation and resuspended in Buffer A (50 mM Na_2HPO_4, 300 mM NaCl, pH 7.2). Cells were lysed using a French press (EmulsiFlex-C5, Avestin). Proteins were purified using gravity flow columns containing His60 Ni-NTA resin followed by Streptactin or StreptactinXT affinity chromatography. Protein was used fresh or flash-frozen in liquid N_2 in Streptactin elution buffer (BRB80 (80 mM PIPES-KOH, pH 6.8, 1 mM EGTA, 1mM MgCl2) + 2.5mM DTB + 10% glycerol).

Protein was used fresh or flash-frozen in liquid N2 in Streptactin elution buffer (BRB80 + 2.5mM DTB + 10% glycerol). Tubulin was purified from bovine brains as previously described (Ashford and Hyman, 2006) with the modification of using Fractogel EMD SO_3-(M) resin instead of phosphocellulose. Tubulin was labeled using ATTO 633 NHS-ester or TAMRA as described (Hyman et al., 1991). An additional cycle of polymerization/depolymerization was performed before use. Protein concentrations were determined using a DS-11 FX spectrophotometer (DeNovix). Purity of all protein reagents was determined using SDS-PAGE as well as MS for tubulin.

Microtubule Growth Assay—Imaging chambers were constructed using silanized coverglass (18-mm and 22-mm) and double-stick tape as described previously (Bechstedt and Brouhard, 2012; Gell et al., 2010). GMPCPP-stabilized seeds were polymerized from TAMRA-labeled and unlabeled (1:4) tubulin. Growth from seeds was observed by introducing 6% Atto633-tubulin in the presence or absence of 50 nM TPPP-mNeonGreen in imaging buffer (BRB80 supplemented with 1 mM GTP, 0.1 mg/ml BSA, 1% 2-mercaptoethanol, 250 nM glucose oxidase, 64 nM catalase, and 40 mM D-glucose). Time-lapse images were recorded at 10 s intervals using a Zeiss Microscope (Axiovert Z1, 100× 1.45 NA Plan-achromate objective heated to 35°C) with TIRF laser illumination (iLAS2, BioVision) and Prime95B CMOS camera (Photometrics). Microtubule growth rates were analyzed using FIJI/ImageJ (Schindelin et al., 2012).

On-Bead Microtubule Nucleation Assay—Imaging chambers were constructed as they were in the microtubule growth assay. Channels were prepared by flowing SiMAG-IDA/Nickel 1-μm beads diluted 1:50 in BRB80 followed by blocking with 5% Pluronic F-127. Microtubule nucleation from beads was observed by introducing 15 μM tubulin (including

6% Atto633-tubulin) in the presence 1 µM TPPP in imaging buffer. Images were recorded as described above.

For supplementary figure, beads were imaged using differential interference contrast (DIC) with a Prime95B CMOS camera (Photometrics). DIC images were processed with the Pseudo Flat-Field Correction Hadim plugin for ImageJ for better microtubule and bead visualization.

Oligodendrocyte Lysate Nucleation Assay—~5 million OPCs were electroporated with the TPPP-GFP construct, then differentiated for DIV3–4. Cells were treated for 90 min with 10 µg/mL nocodazole, then scraped with a plastic policeman in lysis buffer (0.1% Triton X-100, 10mM DTT, 8mM beta-mercaptoethanol in P12 (12mM PIPES, 2mM $MgCl_2$, 1mM EGTA, pH6.8)). Lysates were spun at 15,000× g and supernatants were combined with 15µM tubulin (1:25 rhodamine-tubulin and unlabeled tubulin), with or without 1mM GTP, then imaged in a chamber as described for the microtubule growth assay using a TIRF microscope (Nikon Eclipse-TI) and an Andor Neo sCMOS camera.

Immunohistochemical Staining—Mice were perfused with 4% paraformaldehyde. Dissected brains were fixed in 4% paraformaldehyde at 4°C for at least 3 h, equilibrated in 30% sucrose overnight at 4°C.

For thin sections, brains were mounted in Tissue-Plus O.C.T. Compound and cryosectioned to 12-µm thick slices. Cryosections were permeabilized with 0.1% Triton X-100 for 3 min at room temperature, then blocked with 10% of goat or donkey serum for 30 min. Cryosections then were incubated with primary antibody against MBP (1:100) at 4°C overnight. Images were acquired at 5× on an epifluorescence microscope (Zeiss Axio Imager M1). Images were stitched together using the Photomerge function in Adobe Photoshop and placed on a black background.

For thick floating sections, brains were then sectioned at 40-µm thickness in sagittal orientation using a sliding microtome (Leica) and stored until staining in glycerol cryoprotectant (30% glycerol, 30% ethylene glycol, 10% PB (phosphate buffer; 0.2M anhydrous Na_2HPO_4, NaH_2PO_4 monohydrate, pH7.4). For immunostaining, sections were first blocked for 1 h at room temperature in 5% donkey serum diluted in PBST (0.3 % Triton X-100 in PBS), then incubated at 4°C overnight with primary antibody (anti-MBP) diluted 1:100 in staining buffer (1% donkey serum in PBST). On the next day, sections were rinsed at room temperature 3 times for 10 min each in staining buffer, then incubated for 2 h at room temperature with secondary antibody conjugated to Alexa Fluor 488. 0.2-µm z-stacks were acquired on a spinning-disk confocal (Nikon Eclipse-TI inverted microscope with Yokogawa spinning disk) with a Photometrics Prime94B sCMOS camera.

EM and Immuno-EM—Mice were perfused with Karlsson-Schultz fixative buffer (4% paraformaldehyde, 2.5% glutaraldehyde) and prepared for EM as previous described (Schultz and Karlsson, 1965). All images were obtained at the Stanford Cell Sciences Imaging Facility on a 120kV TEM (JEOL JEM1400) with a 10.7-megapixel CCD camera (Gatan Orius).

In the P14 spinal cord experiment, oligodendrocytes were identified based on their distinct morphology, including having large nuclei containing optically dense speckled regions and processes containing many optically dense granules (ribosomes). The g-ratio was calculated from measurements taken in FIJI using the formula: g-ratio = d/D, where d is the inner axonal diameter and D is the outer total diameter of the myelin.

For immuno-EM, 300 mesh copper grid with Formvar and carbon coating were glow discharged for 20 s in a Denton Desktop Turbo III vacuum system, then covered with 5 μL of sample and allowed to adsorb for 3 min. Grids were then floated sequentially on drops of the following with PBS washes in between: blocking buffer (0.5% BSA and 0.5% ovalbumin in PBST) for 10 min, anti-TPPP antibody (1:100 in blocking buffer) for 15 min, 5-nm gold beads conjugated to goat anti-rabbit secondary antibody (Electron Microscopy Sciences, EM.GAR5) for 30 min. Grids were fixed in 8% glutaraldehyde for 5 min then stained with 1% uranyl acetate for 1 min prior to imaging.

Rotarod Assay—All mice were handled blinded to genotype. Mice were tested on the Rotarod (Ugo Basile, Milan, Italy) for 3 consecutive days. Mice were tested for 3 trials per day with at least 5 min of rest between trials. On Day 1, mice were first acclimated to the Rotarod at 2 rpm for 60 s, followed by 300 s with acceleration from 2 rpm to 20 rpm. On Day 2, the accelerating paradigm was altered to 4–40 rpm over 300 s. On Day 3, the Rotarod was kept at a constant speed of 32 rpm over 300 s. Latency to fall from the Rotarod was recorded and averaged for each trial day for each genotype.

QUANTIFICATION AND STATISTICAL ANALYSIS

Kymograph Analysis of Live-cell Microscopy—Kymographs were generated using the Multiple Kymographs plugin on FIJI and individual EB3 events were traced using the segmented line selector tool to yield starting and end coordinates, which were used to calculate direction, speed, and duration. At least 2 kymographs were generated for each cell imaged and all EB3 events were averaged for each cell. Kymographs are represented with x-axes oriented with proximal processes on the left and distal processes on the right and y-axes oriented with time at the beginning of the movie on the top and time at the end of the movie on the bottom. Kymographs were analyzed manually using the line segment and measure tools on FIJI. For flux analysis, the distal process was defined as >15 μm from the cell body; this distance was determined based on Sholl analysis results that TPPP KO mouse oligodendrocyte have more processes at distances < 15 μm, which may represent the range that microtubules from the cell body are able to compensate for TPPP loss.

For probability analysis, the actual rate of EB3 plus-ends emanating from ManII+ or TPPP+ puncta (calculated as a fraction of all EB3 arising in the kymograph) was compared to the theoretical or random probability (calculated as the fraction of kymograph width occupied by ManII+ or TPPP+ puncta out of the total kymograph width). The actual rate and random probability were then compared using a paired t-test.

Sholl Analysis and Other Image Analyses of Immunocytochemical Staining—For Sholl analysis, images of tubulin stained oligodendrocytes were traced with Adobe Photoshop using the brush or pencil tool with a 5-pixel round tip and processed into binary images. The freehand tool in FIJI was used to define the cell body in order to calculate a center of mass and cell body radius. These coordinates and binary images were input into the Sholl Analysis plugin on FIJI and analyzed with a radius step size of 5μm. For analysis and representation, some images were placed on a black background with equal pixel size/area.

For primary process thickness measurements, processes were measured using the line tool in FIJI at the exit site from the cell body, tangential to the circumference of the cell body.

For branchpoint analysis, GM130+ puncta were defined as being located at a branchpoint if the center of mass of the puncta was ≤ 1 μm away from the intersection of 2 or more microtubules.

For quantification of number of GM130+ puncta in mouse oligodendrocytes, samples were imaged on SIM microscope. Many TPPP KO oligodendrocyte GM130+ puncta appear to be clumps of Golgi outside the cell body in close proximity to each other; therefore one Golgi outpost was quantified as being 2 μm away from adjacent Golgi outposts.

In 2D oligodendrocytes visualized with smFISH, co-stained MBP protein intensity was quantified using the Intensity Density measurement function of ImageJ/FIJI. Each cell boundary was traced using the freehand tool then measured for area and intensity density. Intensity density values were divided by the total area, then normalized against the control (WT) values.

MS Quantification—Proteins with greater than 1 hit in the TPPP IP across all 3 trials were retained. Nonspecifically associated proteins with more hits in the anti-GFP eluate than the anti-TPPP eluate were filtered out during data analysis. Average fold enrichment was calculated from the ratio between TPPP IP hits versus Golgi input hits; for proteins with 0 Golgi hits, this ratio was set to the number of TPPP IP hits since it is not possible to divide by 0; proteins with average fold enrichment below 1 were eliminated. Proteins were sorted by normalized enrichment factor where an enrichment factor of 1 was assigned to the protein with the most number of hits in each trial.

Immunohistochemical Staining Quantification—For thin sections, intensity analysis was performed on ImageJ/FIJI using the freehand tool to trace brain region boundaries and measured using the histogram tool. Average intensity per brain region was calculated from the sum of all pixel intensities in each region divided by the total number of pixels in each region.

For thick sections, confocal stacks were analyzed using Neurolucida 360 software. Images were opened in the 3D environment, then the “tree” user-guided tracing mode with the Directional Kernels algorithm was used to trace individual myelin sheaths. DAT files of tracings of each image were generated, then analyzed in the Neurolucida Explorer software using the individual tree method. Data was then exported into Microsoft Excel files for analysis of number of myelin sheaths, length of each individual sheath, total sheath length (μm), and area/radius.

Statistical Analysis—The n number for each experiment and details of statistical analyses are described in the figure legends or main text.

All data and error bars are presented as mean ± SEM (unless otherwise indicated). All p-values are from two-tailed Student's t-tests (unless otherwise indicated). Significance was defined with the following notations: n.s. not significant, * $p < 0.05$, ** $p < 0.01$, *** $p < 0.001$.

All statistical analyses were performed with GraphPad Prism 8 software (unless otherwise indicated).

DATA AND CODE AVAILABILITY

The published article includes all datasets generated during this study.

Supplementary Material

Refer to Web version on PubMed Central for supplementary material.

ACKNOWLEDGEMENTS

We are grateful for mentorship from William Talbot, Thomas Clandinin, Mary Hynes, Marc Tessier-Lavigne, technical assistance from Cheng-Yun Lee, Madhuri Nori, Lynn Serizawa, advice on EM technique and interpretation from Steve Scherer, Jian Li, Ian Duncan, advice on microfiber cultures from the Charles ffrench-Constant Lab (Marie Bechler). We thank Stanford core facilities: Transgenic Center (Hong Zeng), Neuroscience Microscopy Service (Andrew Olson, NIH NS069375), Cell Sciences Imaging Facility (Anum Khan, Jon Mulholland, National Center for Research Resources (NCRR) 1S10OD01227601), MS Core (Chris Adams, Ryan Leibs), Behavioral and Functional Neuroscience Laboratory (Mehrdad Shamloo, Nay Saw). We thank the Microbiology Department (Lisa Selzer), the Roger Kornberg Lab (Ralph and Barbara Davis) for ultracentrifuge use, the Thomas Sudhof Lab (Mu Zhou, Karthik Raju) for behavioral equipment use.

Funding sources: M.-m.F. by fellowships from the National Multiple Sclerosis Society (NMSS), the National Institute of Neurological Disorders and Stroke (NINDS; F32 NS90721), National Institute of Child Health and Human Development (NICHD; T32 HD7249), J.J.P. by a NCRR ARRA Award 1S10RR026780, A.L.B. (Director, UCSF Bio-Organic Biomedical MS Resource) by the National Institute of General Medical Sciences (NIGMS; P41 GM103481), S.B. by NSERC RGPIN-2017-04649 and CIHR PJT-156193. We are especially grateful to the Dr. Miriam and Sheldon G. Adelson Medical Research Foundation (B.A.B., A.L.B.) and the Myra Reinhard Foundation (B.A.B.); we could not have finished this research without their funding.

We acknowledge the mentorship and friendship of Ben Barres, who dedicated his life to making fundamental discoveries in glial cell biology and advocating for underrepresented people in science. We miss him very much.

REFERENCES

Ashford AJ, and Hyman AA (2006). Chapter 22 - Preparation of Tubuin from Porcine Brain In Cell Biology, Celis JE, ed. (Burlington: Academic Press), pp. 155–160.

Baas PW, Deitch JS, Black MM, and Banker GA (1988). Polarity orientation of microtubules in hippocampal neurons: uniformity in the axon and nonuniformity in the dendrite. Proc Natl Acad Sci U S A 85, 8335–8339. [PubMed: 3054884]

Baraban M, Koudelka S, and Lyons DA (2018). Ca (2+) activity signatures of myelin sheath formation and growth in vivo. Nat Neurosci 21, 19–23. [PubMed: 29230058]

Bechler ME, Byrne L, and Ffrench-Constant C (2015). CNS Myelin Sheath Lengths Are an Intrinsic Property of Oligodendrocytes. Curr Biol 25, 2411–2416. [PubMed: 26320951]

Bechstedt S, and Brouhard GJ (2012). Doublecortin recognizes the 13-protofilament microtubule cooperatively and tracks microtubule ends. Dev Cell 23, 181–192. [PubMed: 22727374]

Burton PR, and Paige JL (1981). Polarity of axoplasmic microtubules in the olfactory nerve of the frog. Proc Natl Acad Sci U S A 78, 3269–3273. [PubMed: 6973153]

Carson JH, Worboys K, Ainger K, and Barbarese E (1997). Translocation of myelin basic protein mRNA in oligodendrocytes requires microtubules and kinesin. Cell motility and the cytoskeleton 38, 318–328. [PubMed: 9415374]

Chabin-Brion K, Marceiller J, Perez F, Settegrana C, Drechou A, Durand G, and Pous C (2001). The Golgi complex is a microtubule-organizing organelle. Mol Biol Cell 12, 2047–2060. [PubMed: 11452002]

Chong SY, Rosenberg SS, Fancy SP, Zhao C, Shen YA, Hahn AT, McGee AW, Xu X, Zheng B, Zhang LI, et al. (2012). Neurite outgrowth inhibitor Nogo-A establishes spatial segregation and extent of oligodendrocyte myelination. Proc Natl Acad Sci U S A 109, 1299–1304. [PubMed: 22160722]

Clauser KR, Baker P, and Burlingame AL (1999). Role of accurate mass measurement (+/− 10 ppm) in protein identification strategies employing MS or MS/MS and database searching. Analytical chemistry 71, 2871–2882. [PubMed: 10424174]

Court FA, Sherman DL, Pratt T, Garry EM, Ribchester RR, Cottrell DF, Fleetwood-Walker SM, and Brophy PJ (2004). Restricted growth of Schwann cells lacking Cajal bands slows conduction in myelinated nerves. Nature 431, 191–195. [PubMed: 15356632]

de Vries H, Schrage C, Hoekstra K, Kok JW, van der Haar ME, Kalicharan D, Liem RS, Copray JC, and Hoekstra D (1993). Outstations of the Golgi complex are present in the processes of cultured rat oligodendrocytes. J Neurosci Res 36, 336–343. [PubMed: 8271312]

Dugas JC, and Emery B (2013). Purification of oligodendrocyte precursor cells from rat cortices by immunopanning. Cold Spring Harbor protocols 2013, 745–758. [PubMed: 23906908]

Duncan ID, Bugiani M, Radcliff AB, Moran JJ, Lopez-Anido C, Duong P, August BK, Wolf NI, van der Knaap MS, and Svaren J (2017). A mutation in the Tubb4a gene leads to microtubule accumulation with hypomyelination and demyelination. Ann Neurol 81, 690–702. [PubMed: 28393430]

Edgar JM, McLaughlin M, Werner HB, McCulloch MC, Barrie JA, Brown A, Faichney AB, Snaidero N, Nave KA, and Griffiths IR (2009). Early ultrastructural defects of axons and axon-glia junctions in mice lacking expression of Cnp1. Glia 57, 1815–1824. [PubMed: 19459211]

Edgar JM, McLaughlin M, Yool D, Zhang SC, Fowler JH, Montague P, Barrie JA, McCulloch MC, Duncan ID, Garbern J, et al. (2004). Oligodendroglial modulation of fast axonal transport in a mouse model of hereditary spastic paraplegia. J Cell Biol 166, 121–131. [PubMed: 15226307]

Efimov A, Kharitonov A, Efimova N, Loncarek J, Miller PM, Andreyeva N, Gleeson P, Galjart N, Maia AR, McLeod IX, et al. (2007). Asymmetric CLASP-dependent nucleation of noncentrosomal microtubules at the trans-Golgi network. Dev Cell 12, 917–930. [PubMed: 17543864]

Emery B, and Dugas JC (2013). Purification of oligodendrocyte lineage cells from mouse cortices by immunopanning. Cold Spring Harbor protocols 2013, 854–868. [PubMed: 24003195]

Farber-Katz SE, Dippold HC, Buschman MD, Peterman MC, Xing M, Noakes CJ, Tat J, Ng MM, Rahajeng J, Cowan DM, et al. (2014). DNA damage triggers Golgi dispersal via DNA-PK and GOLPH3. Cell 156, 413–427. [PubMed: 24485452]

Fruhbeis C, Frohlich D, Kuo WP, Amphornrat J, Thilemann S, Saab AS, Kirchhoff F, Mobius W, Goebbels S, Nave KA, et al. (2013). Neurotransmitter-triggered transfer of exosomes mediates oligodendrocyte-neuron communication. PLoS biology 11, e1001604. [PubMed: 23874151]

Frykman S, Teranishi Y, Hur JY, Sandebring A, Yamamoto NG, Ancarcrona M, Nishimura T, Winblad B, Bogdanovic N, Schedin-Weiss S, et al. (2012). Identification of two novel synaptic gamma-secretase associated proteins that affect amyloid beta-peptide levels without altering Notch processing. Neurochemistry international 61, 108–118. [PubMed: 22521230]

Furusho M, Dupree JL, Nave KA, and Bansal R (2012). Fibroblast growth factor receptor signaling in oligodendrocytes regulates myelin sheath thickness. J Neurosci 32, 6631–6641. [PubMed: 22573685]

Gell C, Bormuth V, Brouhard GJ, Cohen DN, Diez S, Friel CT, Helenius J, Nitzsche B, Petzold H, Ribbe J, et al. (2010). Microtubule dynamics reconstituted in vitro and imaged by single-molecule fluorescence microscopy. Methods Cell Biol 95, 221–245. [PubMed: 20466138]

Gibson EM, Purger D, Mount CW, Goldstein AK, Lin GL, Wood LS, Inema I, Miller SE, Bieri G, Zuchero JB, et al. (2014). Neuronal activity promotes oligodendrogenesis and adaptive myelination in the mammalian brain. Science 344, 1252304. [PubMed: 24727982]

Gimpel P, Lee YL, Sobota RM, Calvi A, Koullourou V, Patel R, Mamchaoui K, Nedelec F, Shackleton S, Schmoranzer J, et al. (2017). Nesprin-1alpha-Dependent Microtubule Nucleation from the Nuclear Envelope via Akap450 Is Necessary for Nuclear Positioning in Muscle Cells. Curr Biol 27, 2999–3009 e2999. [PubMed: 28966089]

Goldbaum O, Jensen PH, and Richter-Landsberg C (2008). The expression of tubulin polymerization promoting protein TPPP/p25alpha is developmentally regulated in cultured rat brain oligodendrocytes and affected by proteolytic stress. Glia 56, 1736–1746. [PubMed: 18563798]

Guan S, Price JC, Prusiner SB, Ghaemmaghami S, and Burlingame AL (2011). A data processing pipeline for mammalian proteome dynamics studies using stable isotope metabolic labeling. Mol Cell Proteomics 10, M111 010728.

Gunn PA, Gliddon BL, Londrigan SL, Lew AM, van Driel IR, and Gleeson PA (2011). The Golgi apparatus in the endomembrane-rich gastric parietal cells exist as functional stable mini-stacks dispersed throughout the cytoplasm. Biology of the cell 103, 559–572. [PubMed: 21899517]

Guzik-Lendrum S, Nagy A, Takagi Y, Houdusse A, and Sellers JR (2011). Drosophila melanogaster myosin-18 represents a highly divergent motor with actin tethering properties. J Biol Chem 286, 21755–21766. [PubMed: 21498886]

Herbert AL, Fu MM, Drerup CM, Gray RS, Harty BL, Ackerman SD, O'Reilly-Pol T, Johnson SL, Nechiporuk AV, Barres BA, et al. (2017). Dynein/dynactin is necessary for anterograde transport of Mbp mRNA in oligodendrocytes and for myelination in vivo. Proc Natl Acad Sci U S A 114, E9153–E9162. [PubMed: 29073112]

Hoftberger R, Fink S, Aboul-Enein F, Botond G, Olah J, Berki T, Ovadi J, Lassmann H, Budka H, and Kovacs GG (2010). Tubulin polymerization promoting protein (TPPP/p25) as a marker for oligodendroglial changes in multiple sclerosis. Glia 58, 1847–1857. [PubMed: 20737479]

Horton AC, Racz B, Monson EE, Lin AL, Weinberg RJ, and Ehlers MD (2005). Polarized secretory trafficking directs cargo for asymmetric dendrite growth and morphogenesis. Neuron 48, 757–771. [PubMed: 16337914]

Hughes EG, Orthmann-Murphy JL, Langseth AJ, and Bergles DE (2018). Myelin remodeling through experience-dependent oligodendrogenesis in the adult somatosensory cortex. Nat Neurosci 21, 696–706. [PubMed: 29556025]

Hyman A, Drechsel D, Kellogg D, Salser S, Sawin K, Steffen P, Wordeman L, and Mitchison T (1991). Preparation of modified tubulins. Methods in enzymology 196, 478–485. [PubMed: 2034137]

Kohl R, Antoine M, Olwin BB, Dickson C, and Kiefer P (2000). Cysteine-rich fibroblast growth factor receptor alters secretion and intracellular routing of fibroblast growth factor 3. J Biol Chem 275, 15741–15748. [PubMed: 10748074]

Koudelka S, Voas MG, Almeida RG, Baraban M, Soetaert J, Meyer MP, Talbot WS, and Lyons DA (2016). Individual Neuronal Subtypes Exhibit Diversity in CNS Myelination Mediated by Synaptic Vesicle Release. Curr Biol 26, 1447–1455. [PubMed: 27161502]

Kovacs GG, Laszlo L, Kovacs J, Jensen PH, Lindersson E, Botond G, Molnar T, Perczel A, Hudecz F, Mezo G, et al. (2004). Natively unfolded tubulin polymerization promoting protein TPPP/p25 is a common marker of alpha-synucleinopathies. Neurobiology of disease 17, 155–162. [PubMed: 15474353]

Kunkel TA (1985). Rapid and efficient site-specific mutagenesis without phenotypic selection. Proc Natl Acad Sci U S A 82, 488–492. [PubMed: 3881765]

Lin JP, Mironova YA, Shrager P, and Giger RJ (2017). LRP1 regulates peroxisome biogenesis and cholesterol homeostasis in oligodendrocytes and is required for proper CNS myelin development and repair. eLife 6.

Lindersson E, Lundvig D, Petersen C, Madsen P, Nyengaard JR, Hojrup P, Moos T, Otzen D, Gai WP, Blumbergs PC, et al. (2005). p25alpha Stimulates alpha-synuclein aggregation and is co-localized with aggregated alpha-synuclein in alpha-synucleinopathies. J Biol Chem 280, 5703–5715. [PubMed: 15590652]

Liu J, Dietz K, DeLoyht JM, Pedre X, Kelkar D, Kaur J, Vialou V, Lobo MK, Dietz DM, Nestler EJ, et al. (2012). Impaired adult myelination in the prefrontal cortex of socially isolated mice. Nat Neurosci 15, 1621–1623. [PubMed: 23143512]

Lunn KF, Baas PW, and Duncan ID (1997). Microtubule organization and stability in the oligodendrocyte. J Neurosci 17, 4921–4932. [PubMed: 9185530]

Nguyen MM, McCracken CJ, Milner ES, Goetschius DJ, Weiner AT, Long MK, Michael NL, Munro S, and Rolls MM (2014). Gamma-tubulin controls neuronal microtubule polarity independently of Golgi outposts. Mol Biol Cell 25, 2039–2050. [PubMed: 24807906]

Norholm MH (2010). A mutant Pfu DNA polymerase designed for advanced uracil-excision DNA engineering. BMC biotechnology 10, 21. [PubMed: 20233396]

Oddoux S, Zaal KJ, Tate V, Kenea A, Nandkeolyar SA, Reid E, Liu W, and Ralston E (2013). Microtubules that form the stationary lattice of muscle fibers are dynamic and nucleated at Golgi elements. J Cell Biol 203, 205–213. [PubMed: 24145165]

Ori-McKenney KM, Jan LY, and Jan YN (2012). Golgi outposts shape dendrite morphology by functioning as sites of acentrosomal microtubule nucleation in neurons. Neuron 76, 921–930. [PubMed: 23217741]

Peranen J, Rikkonen M, Hyvonen M, and Kaariainen L (1996). T7 vectors with modified T7lac promoter for expression of proteins in Escherichia coli. Analytical biochemistry 236, 371–373. [PubMed: 8660525]

Perrin J, Mortier M, Jacomin AC, Viargues P, Thevenon D, and Fauvarque MO (2015). The nonaspanins TM9SF2 and TM9SF4 regulate the plasma membrane localization and signalling activity of the peptidoglycan recognition protein PGRP-LC in Drosophila. Journal of innate immunity 7, 37–46. [PubMed: 25139117]

Petry S, Groen AC, Ishihara K, Mitchison TJ, and Vale RD (2013). Branching microtubule nucleation in Xenopus egg extracts mediated by augmin and TPX2. Cell 152, 768–777. [PubMed: 23415226]

Procter DJ, Banerjee A, Nukui M, Kruse K, Gaponenko V, Murphy EA, Komarova Y, and Walsh D (2018). The HCMV Assembly Compartment Is a Dynamic Golgi-Derived MTOC that Controls Nuclear Rotation and Virus Spread. Dev Cell 45, 83–100 e107. [PubMed: 29634939]

Quassollo G, Wojnacki J, Salas DA, Gastaldi L, Marzolo MP, Conde C, Bisbal M, Couve A, and Caceres A (2015). A RhoA Signaling Pathway Regulates Dendritic Golgi Outpost Formation. Curr Biol 25, 971–982. [PubMed: 25802147]

Reuter MS, Tawamie H, Buchert R, Hosny Gebril O, Froukh T, Thiel C, Uebe S, Ekici AB, Krumbiegel M, Zweier C, et al. (2017). Diagnostic Yield and Novel Candidate Genes by Exome Sequencing in 152 Consanguineous Families With Neurodevelopmental Disorders. JAMA psychiatry 74, 293–299. [PubMed: 28097321]

Sanchez-Huertas C, Freixo F, Viais R, Lacasa C, Soriano E, and Luders J (2016). Non-centrosomal nucleation mediated by augmin organizes microtubules in post-mitotic neurons and controls axonal microtubule polarity. Nature communications 7, 12187.

Schindelin J, Arganda-Carreras I, Frise E, Kaynig V, Longair M, Pietzsch T, Preibisch S, Rueden C, Saalfeld S, Schmid B, et al. (2012). Fiji: an open-source platform for biological-image analysis. Nat Methods 9, 676–682. [PubMed: 22743772]

Schultz RL, and Karlsson U (1965). Fixation of the Central Nervous System for Electron Microscopy by Aldehyde Perfusion. Ii. Effect of Osmolarity, Ph of Perfusate, and Fixative Concentration. Journal of ultrastructure research 12, 187–206. [PubMed: 14289427]

Simons C, Wolf NI, McNeil N, Caldovic L, Devaney JM, Takanohashi A, Crawford J, Ru K, Grimmond SM, Miller D, et al. (2013). A de novo mutation in the beta-tubulin gene TUBB4A results in the leukoencephalopathy hypomyelination with atrophy of the basal ganglia and cerebellum. American journal of human genetics 92, 767–773. [PubMed: 23582646]

Snaidero N, Mobius W, Czopka T, Hekking LH, Mathisen C, Verkleij D, Goebbels S, Edgar J, Merkler D, Lyons DA, et al. (2014). Myelin membrane wrapping of CNS axons by PI(3,4,5)P3-dependent polarized growth at the inner tongue. Cell 156, 277–290. [PubMed: 24439382]

Song YJ, Lundvig DM, Huang Y, Gai WP, Blumbergs PC, Hojrup P, Otzen D, Halliday GM, and Jensen PH (2007). p25alpha relocalizes in oligodendroglia from myelin to cytoplasmic inclusions in multiple system atrophy. The American journal of pathology 171, 1291–1303. [PubMed: 17823288]

Stearns T, Evans L, and Kirschner M (1991). Gamma-tubulin is a highly conserved component of the centrosome. Cell 65, 825–836. [PubMed: 1840506]

Stepanova T, Slemmer J, Hoogenraad CC, Lansbergen G, Dortland B, De Zeeuw CI, Grosveld F, van Cappellen G, Akhmanova A, and Galjart N (2003). Visualization of microtubule growth in cultured neurons via the use of EB3-GFP (end-binding protein 3-green fluorescent protein). J Neurosci 23, 2655–2664. [PubMed: 12684451]

Takahashi M, Tomizawa K, Fujita SC, Sato K, Uchida T, and Imahori K (1993). A brain-specific protein p25 is localized and associated with oligodendrocytes, neuropil, and fiber-like structures of the CA3 hippocampal region in the rat brain. J Neurochem 60, 228–235. [PubMed: 8417144]

Tirian L, Hlavanda E, Olah J, Horvath I, Orosz F, Szabo B, Kovacs J, Szabad J, and Ovadi J (2003). TPPP/p25 promotes tubulin assemblies and blocks mitotic spindle formation. Proc Natl Acad Sci U S A 100, 13976–13981. [PubMed: 14623963]

Trajkovic K, Dhaunchak AS, Goncalves JT, Wenzel D, Schneider A, Bunt G, Nave KA, and Simons M (2006). Neuron to glia signaling triggers myelin membrane exocytosis from endosomal storage sites. J Cell Biol 172, 937–948. [PubMed: 16520383]

Vincze O, Tokesi N, Olah J, Hlavanda E, Zotter A, Horvath I, Lehotzky A, Tirian L, Medzihradszky KF, Kovacs J, et al. (2006). Tubulin polymerization promoting proteins (TPPPs): members of a new family with distinct structures and functions. Biochemistry 45, 13818–13826. [PubMed: 17105200]

Wang L, and Brown A (2002). Rapid movement of microtubules in axons. Curr Biol 12, 1496–1501. [PubMed: 12225664]

Wang Y, Taguchi T, and Warren G (2006). Purification of Rat Liver Golgi Stacks, Vol 2 (Elsevier).

Yau KW, Schatzle P, Tortosa E, Pages S, Holtmaat A, Kapitein LC, and Hoogenraad CC (2016). Dendrites In Vitro and In Vivo Contain Microtubules of Opposite Polarity and Axon Formation Correlates with Uniform Plus-End-Out Microtubule Orientation. J Neurosci 36, 1071–1085. [PubMed: 26818498]

Ye B, Zhang Y, Song W, Younger SH, Jan LY, and Jan YN (2007). Growing dendrites and axons differ in their reliance on the secretory pathway. Cell 130, 717–729. [PubMed: 17719548]

Zenker J, White MD, Templin RM, Parton RG, Thorn-Seshold O, Bissiere S, and Plachta N (2017). A microtubule-organizing center directing intracellular transport in the early mouse embryo. Science 357, 925–928. [PubMed: 28860385]

Zhang Y, Chen K, Sloan SA, Bennett ML, Scholze AR, O'Keeffe S, Phatnani HP, Guarnieri P, Caneda C, Ruderisch N, et al. (2014). An RNA-sequencing transcriptome and splicing database of glia, neurons, and vascular cells of the cerebral cortex. J Neurosci 34, 11929–11947. [PubMed: 25186741]

Zhou W, Chang J, Wang X, Savelieff MG, Zhao Y, Ke S, and Ye B (2014). GM130 is required for compartmental organization of dendritic golgi outposts. Curr Biol 24, 1227–1233. [PubMed: 24835455]

Zuber ME, Zhou Z, Burrus LW, and Olwin BB (1997). Cysteine-rich FGF receptor regulates intracellular FGF-1 and FGF-2 levels. Journal of cellular physiology 170, 217–227. [PubMed: 9066777]

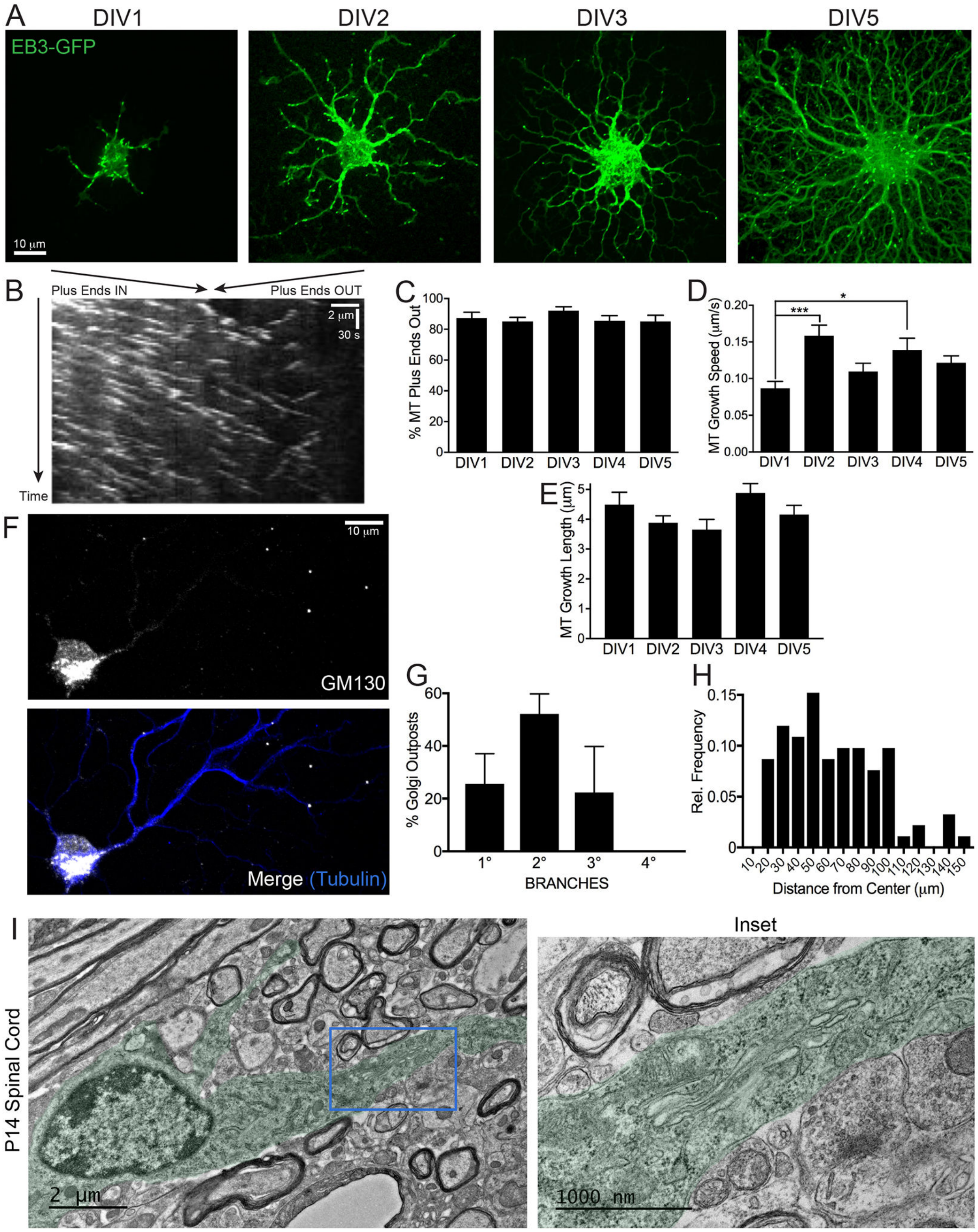

Figure 1. Oligodendrocytes Have Uniform Microtubule Polarity and Golgi Outposts

(A) Confocal micrographs of immunopanned rat primary oligodendrocytes expressing EB3-EGFP and differentiated for 1–5 days in vitro (DIV).

(B) Kymograph from a confocal movie of a DIV2 oligodendrocyte expressing EB3-EGFP.

(C) Percent of microtubule plus-ends labeled with EB3-EGFP that are growing away from the cell body in DIV1–5 oligodendrocytes.

(D) Microtubule growth speeds of EB3-EGFP in DIV1–5 oligodendrocytes. * p = 0.045, *** p = 0.0005.

(E) Microtubule growth lengths of EB3-EGFP in DIV1–5 oligodendrocytes. n = 11–18 cells from 4 biological replicates (4 cultures from 4 rats), mean per cell from 102–354 events (per DIV). One-way ANOVA with post-hoc Tukey's multiple comparisons test.

(F) Confocal micrograph of a rat DIV4 oligodendrocyte immunostained against GM130 and tubulin.

(G) Percent of GM130+ Golgi outposts located along primary, secondary, tertiary, or quaternary processes.

(H) Histogram distribution of GM130+ Golgi outpost locations relative to distance from the center of the cell body. Data did not pass the Shapiro-Wilk normality test, p = 0.0036.

(I) EM from P14 mouse spinal cord of an oligodendrocyte with 2 processes (pseudocolored in green). The thicker process contains a Golgi outpost ~4–6 μm from the cell body with multiple stacks. The blue box in the left image (2000x) is enlarged on the right (8000x). n = 2 mice.

See also Figures S1 and S2, Video 1.

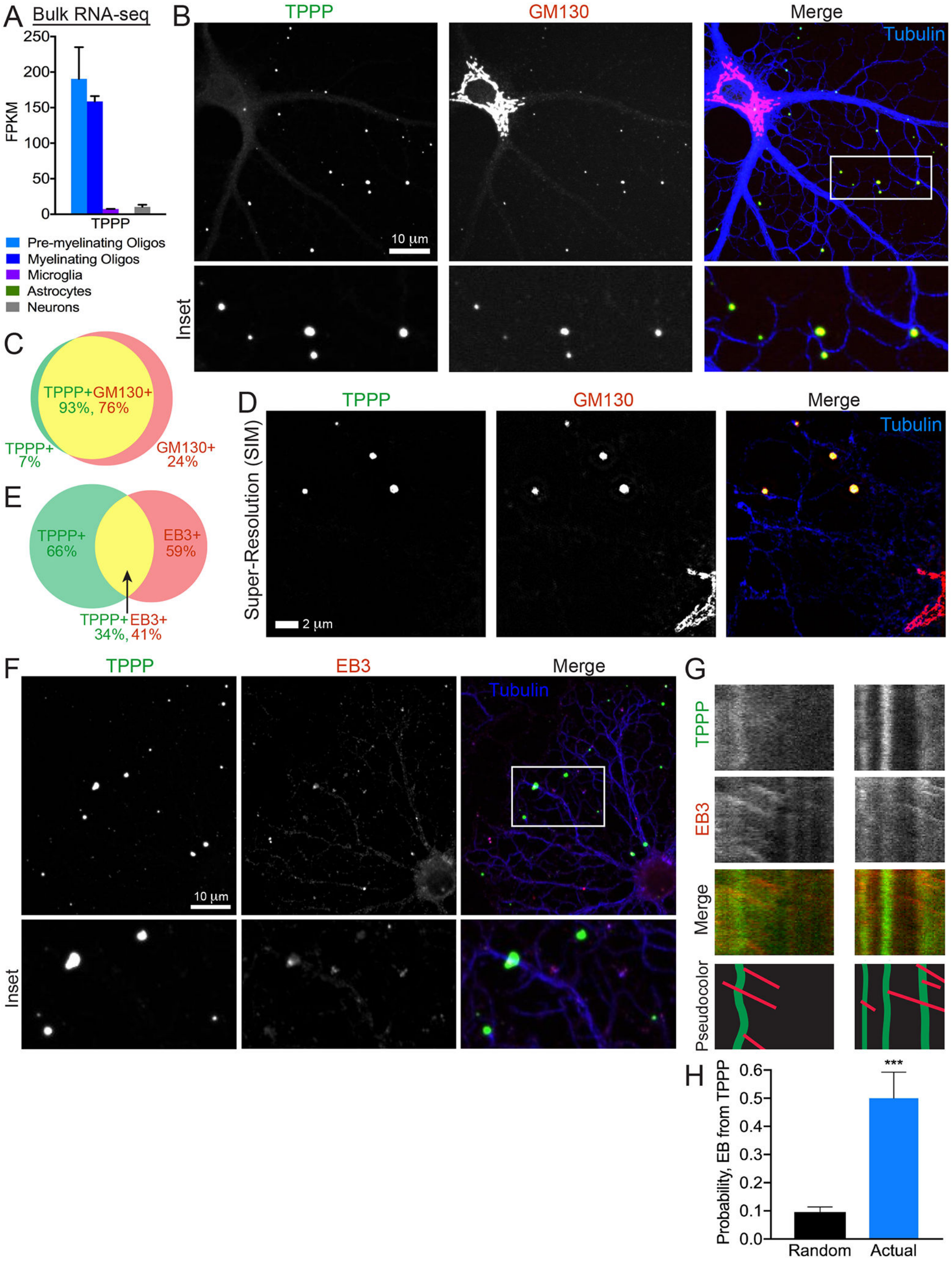

Figure 2. TPPP is a Specific Marker for Golgi Outposts

(A) TPPP mRNA expression from RNA-seq of immunopanned mouse brain cells (Zhang et al., 2014). FPKM (frequency per kilobase million).

(B) Confocal micrograph of a rat DIV4 oligodendrocyte immunostained against TPPP, GM130, and tubulin.

(C) Venn diagram of colocalization relationship between TPPP and GM130 outside the cell body. 93% of TPPP+ puncta colocalize with GM130; 76% of GM130+ puncta colocalize with TPPP.

(D) Super-resolution (structured illumination) micrograph of a rat DIV4 oligodendrocyte immunostained against TPPP, GM130, and tubulin.

(E) Venn diagram of colocalization relationship between TPPP and EB1 outside the cell body. 35% of TPPP+ puncta colocalize with EB1; 41% of EB1+ puncta colocalize with TPPP.

(F) Confocal micrograph of rat DIV4 oligodendrocyte immunostained against tubulin, TPPP, and EB1.

(G) Kymographs from rat DIV1–2 oligodendrocytes expressing TPPP-GFP and mCherry-EB3.

(H) Comparison of actual rates of EB3-positive puncta arising from TPPP+ puncta versus probability based on chance. n = 9 cells, 3 biological replicates.

See also Figure S2.

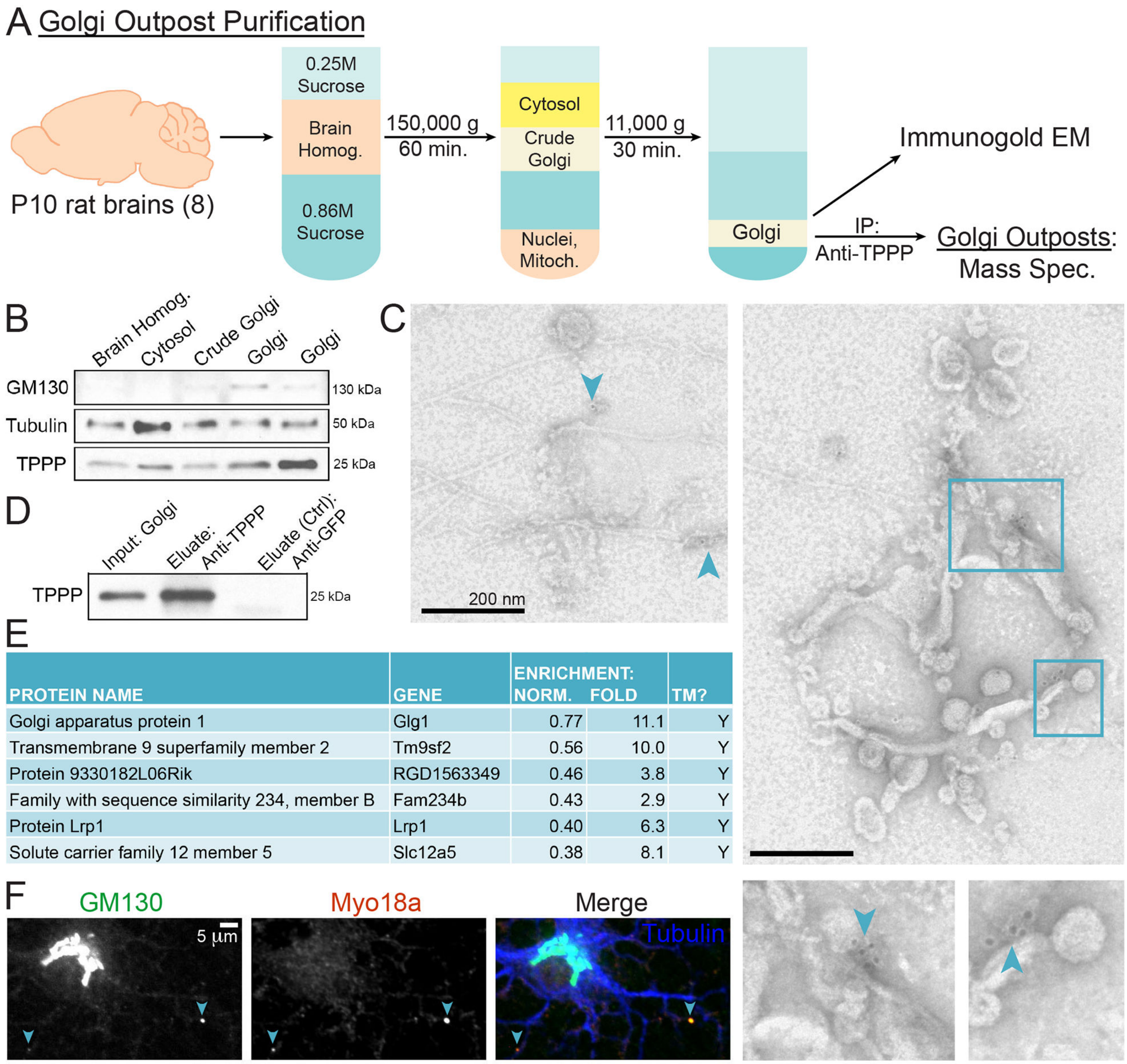

		ENRICHMENT:		
PROTEIN NAME	GENE	NORM.	FOLD	TM?
Golgi apparatus protein 1	Glg1	0.77	11.1	Y
Transmembrane 9 superfamily member 2	Tm9sf2	0.56	10.0	Y
Protein 9330182L06Rik	RGD1563349	0.46	3.8	Y
Family with sequence similarity 234, member B	Fam234b	0.43	2.9	Y
Protein Lrp1	Lrp1	0.40	6.3	Y
Solute carrier family 12 member 5	Slc12a5	0.38	8.1	Y

Figure 3. Purification and Mass Spectrometry of Golgi Outposts

(A) Schematic of Golgi outpost purification from P10 rat brains using differential sucrose-gradient ultracentrifugation. Resulting purified Golgi was then subject to: 1) immuno-EM and 2) IP against TPPP in order to isolate Golgi outposts for MS.

(B) Western blots of Golgi purification fractions show enrichment of GM130 and TPPP. 2 replicates of purified Golgi fractions are shown.

(C) Immuno-EM of purified Golgi that associate with anti-TPPP gold beads. Images show multi-vesicular structures with microtubules emanating from them. Arrowheads point to anti-TPPP gold beads. Bounding boxes are enlarged.

(D) Western blot of anti-TPPP IP using purified Golgi as the input. The negative control used an anti-GFP antibody.

(E) MS of TPPP-associated Golgi outpost proteins. Proteins were sorted by a normalized enrichment value with 1 assigned to the protein with the highest number of spectral counts in each trial. “TM” indicates a protein with transmembrane domain(s) predicted by UniProt. n = 3 biological replicates.

(F) Confocal micrograph of a rat DIV4 oligodendrocyte immunostained against GM130, MYO18A, and tubulin.

See also Figure S3 and Table 1.

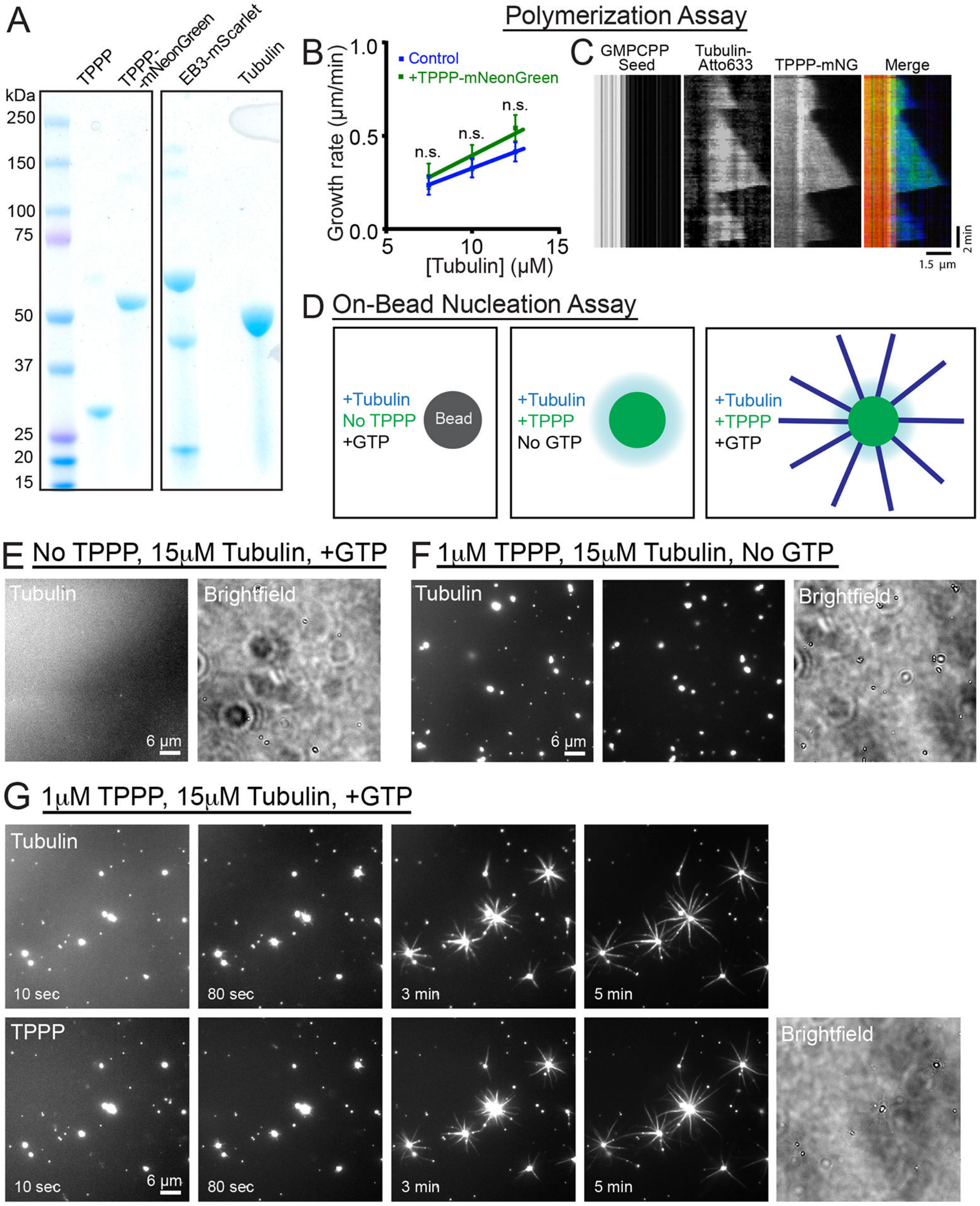

Figure 4. TPPP Nucleates Microtubules

(A) SDS-PAGE gel of purified proteins used in this study.

(B) Microtubule growth rates (of Atto633-tubulin) in the presence of 50 nM TPPP-mNG (mNeon-Green). The control has no TPPP. Data represent mean 00B1 SD (n ≥ 13). Connecting lines represent linear fits indicating association rate constants of 1.02 ± 0.1 μM $^{-1}$*s^{-1} (control) and 1.42 ± 0.2 μM^{-1}*s^{-1} (+TPPP).

(C) Kymograph of polymerization experiment quantified in (B). The merged image is color-coded: TPPP-mNG = green, Atto633-tubulin = blue, stable microtubule seed = red.

(D) Schematic of on-bead nucleation assays.

(E) No-TPPP control: Ni-NTA beads with no TPPP, 15μM tubulin, 1 mM GTP.

(F) No-GTP control: Ni-NTA beads with 1μM TPPP-mNG, 15μM tubulin, no GTP.

(G) Microtubule nucleation from TPPP-beads with 1μM TPPP-mNG, 15μM tubulin, 1 mM GTP.
See also Figure S4, Video 2.

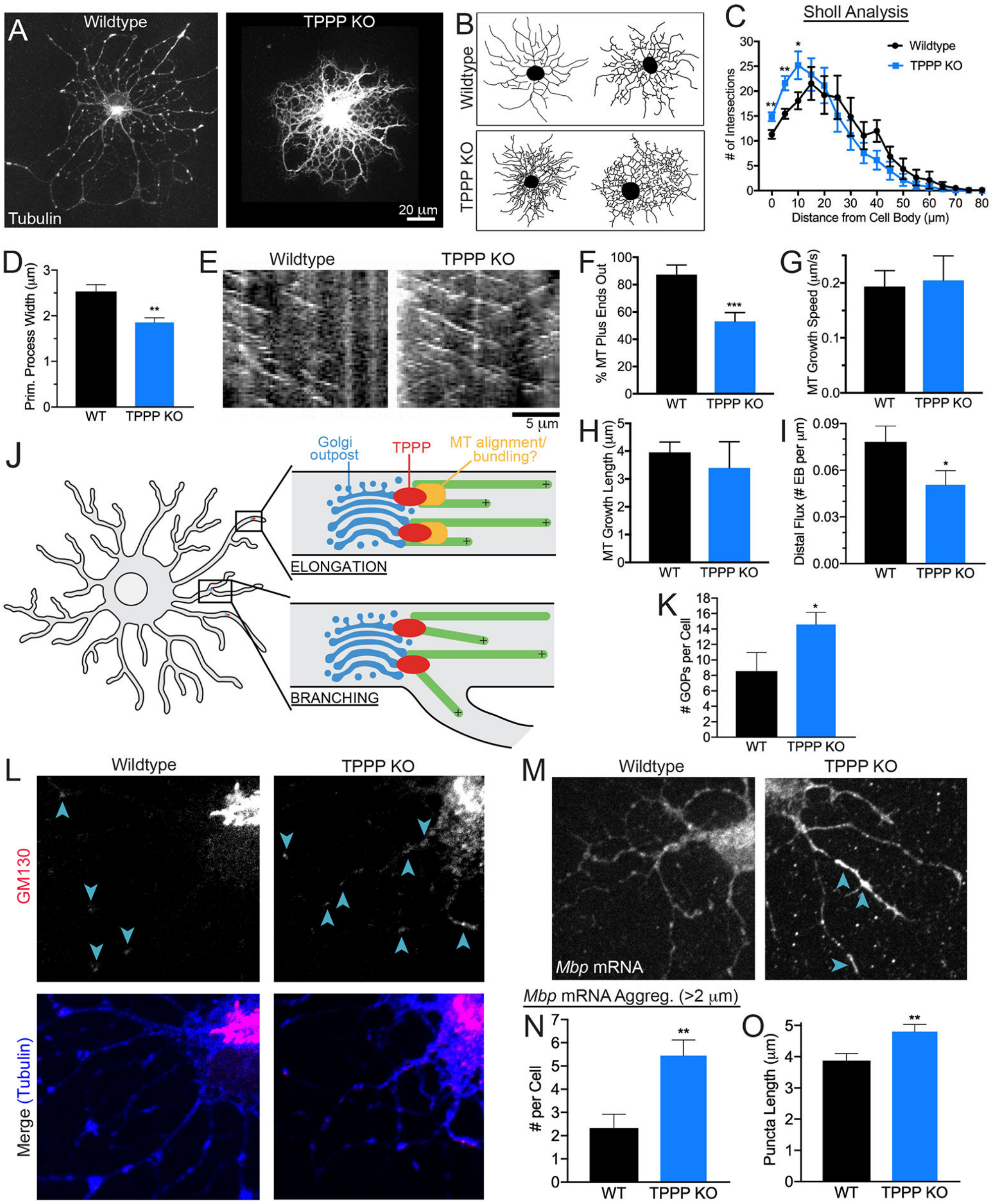

Figure 5. TPPP KO Oligodendrocytes Have Microtubule Organization Defects

(A) Micrographs of DIV4 oligodendrocytes cultured from WT or TPPP KO mice and immunostained against tubulin.

(B) Sample traces of tubulin-stained oligodendrocytes used for Sholl analysis.

(C) Sholl analysis of microtubule processes in WT versus TPPP KO oligodendrocytes.

(D) Width of primary processes. * p = 0.014. n = 13–20 cells, 4 mice per genotype.

(E) Kymographs from WT versus TPPP KO oligodendrocytes expressing mCherry-EB3 (DIV4).

(F) Percent of microtubule plus-ends labeled with mCherry-EB3 that are growing away from the cell body in DIV4 oligodendrocytes. *** $p = 5 \times 10^{-9}$.

(G) Microtubule growth speeds of mCherry-EB3 in DIV4 oligodendrocytes. p = 0.52.

(H) Microtubule growth length of mCherry-EB3 in DIV4 oligodendrocytes. p = 0.11.

(I) Flux of anterograde mCherry-EB3 growing microtubules in distal processes (>15 μm from the cell body). * $p = 0.05$. $n = 9–10$ cells, 3 mice per genotype.

(J) Model for local microtubule polarity and branching regulation at Golgi outposts by TPPP.

(K) Number of Golgi outposts per oligodendrocyte. $n = 11–17$ cells, 3 mice per genotype. * $p = 0.05$.

(L) Micrographs of TPPP KO oligodendrocyte immunostained against GM130 and tubulin.

(M) Micrographs of smFISH against mouse *Mbp* mRNA.

(N) Number of *Mbp* mRNA aggregates with size >2 μm. ** $p = 0.001$.

(O) Size of *Mbp* mRNA aggregates. ** $p = 0.004$. $n = 18–29$ cells, 3 mice per genotype.

See also Figure S5, Video 3.

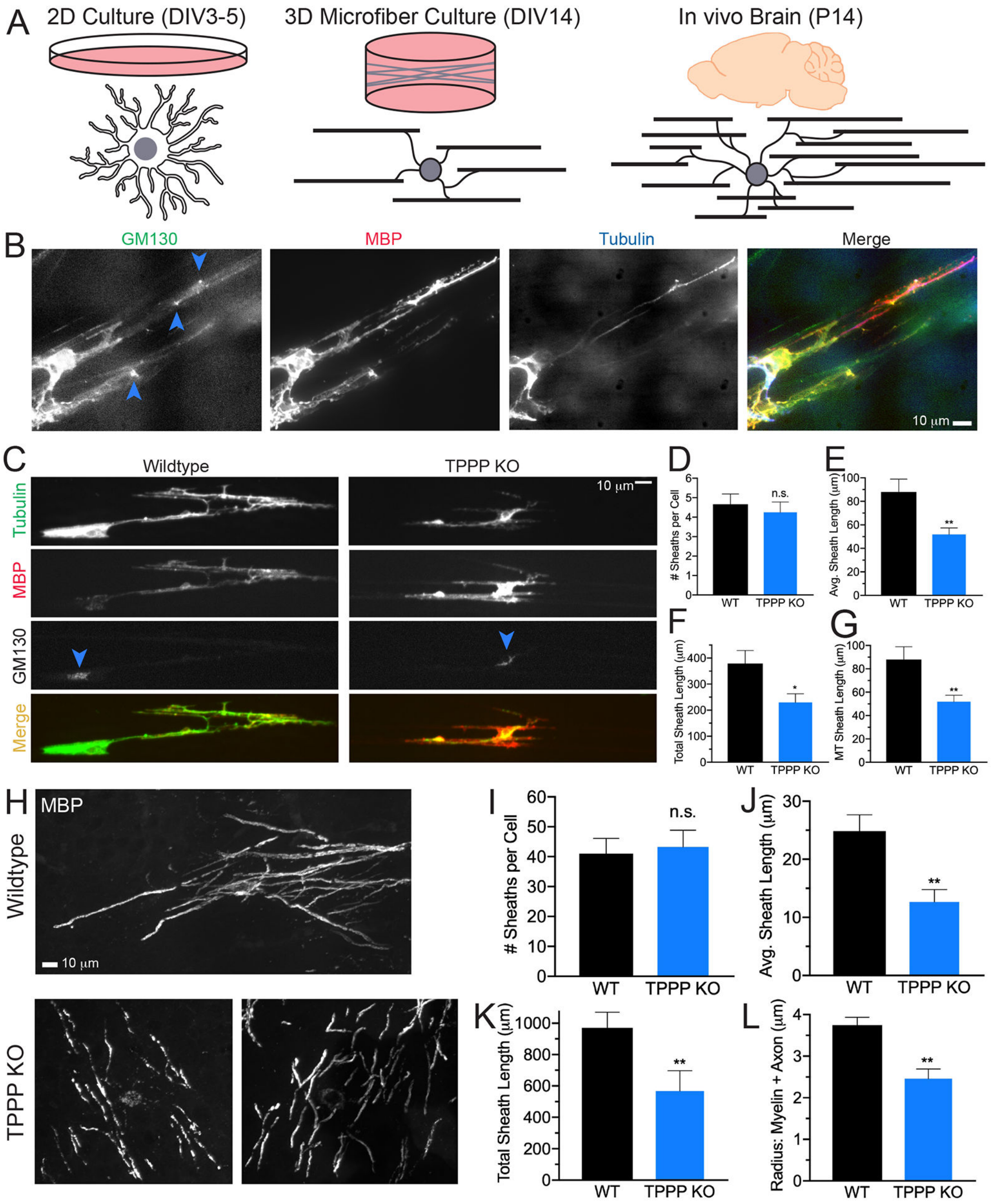

Figure 6. TPPP KO Oligodendrocytes Have Shorter Myelin Sheaths

(A) Schematic of techniques used to discern oligodendrocyte morphology.

(B) Max projections of confocal micrographs (100×) of DIV14 oligodendrocytes cultured from WT or TPPP KO mice on 3D microfibers. Cells were stained against GM130, tubulin, and MBP, then mounted on coverslips. Arrowheads point to Golgi outposts along the myelin sheath.

(C) Max projections (20×) of DIV14 oligodendrocytes cultured on 3D microfibers. Merged images show tubulin and MBP channels. Arrowheads point to cell bodies.

(D) Number of sheaths per cell. p = 0.57.

(E) Average sheath length per cell. ** p = 0.006.

(F) Total sheath length per cell. * p = 0.02.

(G) Microtubule sheath length per cell. ** $p = 0.006$. $n = 3–4$ biological replicates, 21–32 individual cells or cell clusters.

(H) Max projections of confocal micrographs of oligodendrocytes from P14 WT or TPPP KO cortex.

(I) Number of sheaths per cell. $p = 0.77$.

(J) Average sheath length per cell. ** $p = 0.005$.

(K) Total sheath length per cell. * $p = 0.03$.

(L) Combined radius of myelin sheath and axon. ** $p = 0.001$. $n = 3$ mice, 16–23 cells per genotype.

See also Figure S6, Videos 4 and 5.

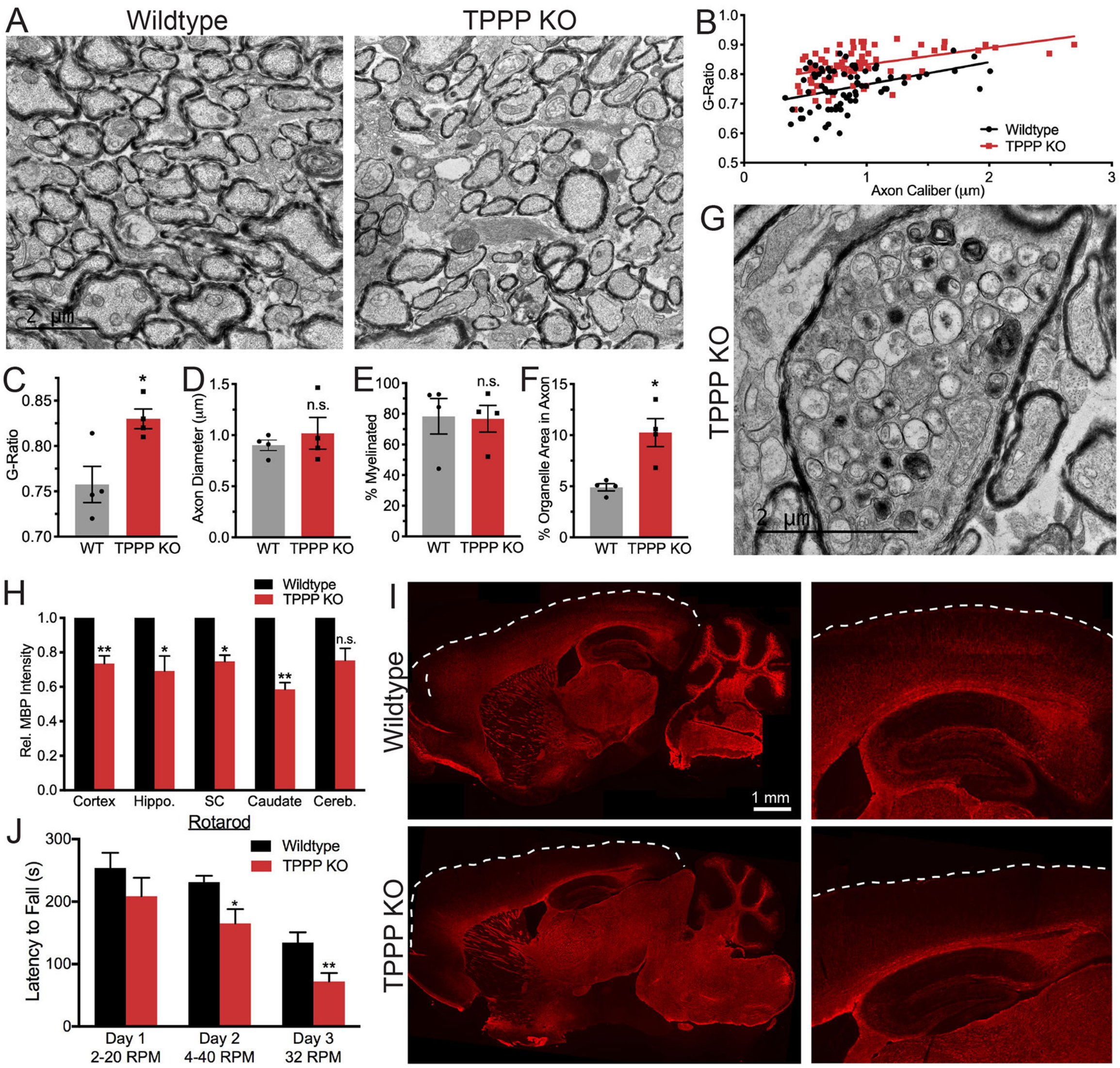

Figure 7. TPPP is Required for Myelination in vivo

(A) EMs (2000x) from 3-months-old mouse optic nerves.

(B) G-ratio scatter plot. Each data point represents one myelinated axon.

(C) G-ratio bar graph. Each data point represents the mean g-ratio per mouse. * p = 0.01.

(D) Axon diameter. p = 0.52.

(E) Percent of myelinated axons. p = 0.80.

(F) Percent of axonal area occupied by organelles. * p = 0.03. n = 4 mice per genotype.

(G) EM image (4000x) from TPPP KO mouse optic nerve with organelle accumulation in the axon.

(H) Quantification of relative MBP staining intensity by brain region. p = 0.009, 0.04, 0.02, 0.015, 0.07.

(I) MBP immunohistochemical staining of 3-months-old mice brains. Right images are zoomed in on hippocampus and cortex. Dashed white line indicates the cortex boundary. n = 4 mice per genotype.

(J) Rotarod behavioral data from 3-months-old mice trained on Day 1 and 2 at variable speeds and tested on Day 3 at constant speed. p = 0.25, 0.02, 0.01. n = 9–10 male mice per genotype.

See also Figure S7.

KEY RESOURCES TABLE

REAGENT or RESOURCE	**SOURCE**	**IDENTIFIER**
Antibodies		
Anti-EB1 (Clone KT51), rat monoclonal	Abcam	Cat#ab53358
Anti-GFP (Clone JL-8), mouse monoclonal	Takara Clontech	Cat#632381
Anti-GM130 (Clone 35), mouse monoclonal	BD Pharmingen	Cat#610822, Cat#560257
Anti-MBP, rat monoclonal	Abcam	Cat#ab7349
Anti-MYO18A, rabbit polyclonal	Sigma	Cat#HPA021121
Anti-TPPP, goat polyclonal (for IP, Western blot)	ThermoFisher Scientific	Cat#PA5–19243
Anti-TPPP, rabbit polyclonal (for staining, immuno-EM)	Proteintech	Cat#18742–1-AP
Anti-α-tubulin (Clone YL1/2), rat monoclonal	ThermoFisher Scientific	Cat#MA1–80017
Anti-α/β-tubulin, sheep polyclonal	Cytoskeleton	Cat#ATN02
Anti-γ-tubulin (Clone DQ-19), rabbit polyclonal	Sigma	Cat#T3195
Anti-γ-tubulin (Clone GTU-88), mouse monoclonal	Sigma	Cat#T5326
Anti-γ-tubulin, rabbit polyclonal	Sigma	Cat#T3559
Anti-γ-tubulin, rabbit polyclonal	Sigma	Cat#T5192
Anti-γ-tubulin (Clone TU-30), mouse polyclonal	Santa Cruz	Cat#sc-51715
Bacterial and Virus Strains		
BL21 (DE3) *E. coli*	NEB	Cat#C2527I
Chemicals, Peptides, and Recombinant Proteins		
His60 Ni-NTA resin	Takara Clontech	Cat#635659
Streptactin or StreptactinXT affinity chromatography	IBA Lifesciences	Cat#2-4998-000
Fractogel EMD SO_3− (M) Resin	EMD Millipore	Cat#1168820010
SiMAG-IDA/Nickel 1-μm Beads	Chemicell	Cat#1512–1
Poly-D-lysine Hydrobromide	Sigma	Cat#P6407
Hibernate A Low Fluorescence Media	BrainBits	Cat#HALF
Dynabeads Protein G for Immunoprecipitation	ThermoFisher Scientific	Cat#10004D
RapiGest SF Surfactant	Waters Corporation	Cat#186001861
Sequencing Grade Modified Trypsin	Promega	Cat#V5113
Porcine Tubulin (for oligodendrocyte lysate nucleation assay)	Cytoskeleton	Cat#T240-A
Rhodamine Porcine Tubulin (for oligodendrocyte lysate nucleation assay)	Cytoskeleton	Cat#TL590M-A
GMPCPP	Jena Bioscience	Cat#NU-405S
TAMRA; 5-(and-6)-Carboxytetramethylrhodamine, Succinimidyl Ester, mixed isomers	ThermoFisher Scientific	Cat#C1171
ATTO 633 NHS-ester	ATTO-TEC	Cat#AD 633–31
Experimental Models: Organisms/Strains		
TPPP knockout mice	Knockout Mouse Project (KOMP)	Cat#VG12652
Wildtype rats, Sprague-Dawley strain	Charles River	N/A

REAGENT or RESOURCE	SOURCE	IDENTIFIER
Oligonucleotides		
smFISH probes against mouse Mbp mRNA CDS, (5’ to 3’): gaagctcgtcggactctgag, ctgtggggtcttcttggatg, gtacttggatcgctgtgagg, atggtccatggtacttgctg, ctgtcaccgctaaagaagcg, taatgggtagttctcgtgtg, gactactgggttttcatctt, ttgggatggaggtggtgttc, caggattcgggaaggctgag, ggcagttatattaagaagcc, actagctaatcggtgcaagt, cgggattaagagagggtctg, atagttttaaccagtcgggg, accccgagaaaactcaatct, ggaacaagtcagggctgaga, aacctccggagtcgaacaag, gtaggggtgaacttggaagg, aaacaaagctctttaggggg, agactgtctgatcctgttag, acaagcccccgttgtataag, acgctcgaaatcagctggtg, acacatatctccagcgtgtt, agagatggtgacatttggcg, cttaaaagcaccagctctgg, accatgagaagtggccagag, ttagtgtgtaccaatgggca, aatggttatttttccaccga, gagtcctttctaggaggcag, gaaccccctaaagctaaga, cagcgactcgattcagtgac, ggacattattagactggggt, agagggataaggaggtgtcg, acagaaggcatgctaaatca, agtgtggggctctttggaag, caagatgcagtattgggcta, ctctactcagagttagaaca, tcggtgttatcttaaaccca, cacgttattgtggcgataca, aaacactcccgtgggacaat, aaggtcgttcagtcacactg, gaatagtaggtgcttctgtc.	LGC Biosearch Technologies	Stellaris RNA Fish, Custom
Recombinant DNA		
Plasmid: tdTomato-MannII-N-10	Addgene	Cat#58110
Plasmid: mCherry-EB3	Gift from Erika Holzbaur	N/A
Plasmid: EB3-EGFP	Gift from Erika Holzbaur	N/A
cDNA: human EB3 (GenBank Accession AY893969)	Harvard PlasmID Database	Plasmid ID: HsCD00331591
cDNA: human TPPP (GenBank Accession BC131506)	Harvard PlasmID Database	Plasmid ID: HsCD00347208
cDNA: rat TPPP	NCBI Reference Sequence	NM_001108461
Plasmid: pHAT2	Addgene	Plasmid ID: 112583
Plasmid: TPPP-mNeonGreen	This paper	N/A
Plasmid: pEGFP-C1	Takara Clontech	Replaced with: Cat#632468
Plasmid: TPPP-EGFP	This paper	N/A
Software and Algorithms		
FIJI/ImageJ	(Schindelin et al., 2012)	Version 2.0.0-rc-69/1.52n; http://fiji.sc
Neurolucida 360	MBF Bioscience	https://www.mbfbioscience.com/neurolucida360
Neurolucida Explorer	MBF Bioscience	https://www.mbfbioscience.com/neurolucida-explorer
Photoshop CS6	Adobe Systems	Version 13.0 ×64
Prism	Graph Pad	Version 8
SoftWoRx	GE Healthcare Life Sciences	DeltaVision Imaging System
Other		
12-well plate containing cell crown inserts of Mimetix aligned fibers (PLLA, 2-micron fiber diameter)	Electrospinning UK via Amsbio	Cat#TECL-006
Tissue-Plus O.C.T. Compound	ThermoFisher Scientific	Cat#23-730-571
VECTASHIELD Antifade Mounting Medium with DAPI	Vector Laboratories	Cat#H-1200
ProLong Gold Antifade Mountant	ThermoFisher Scientific	Cat#P36934
Precision Cover Glasses Thickness No. 1.5H (for super-resolution microscopy)	Marienfeld	Cat#0117520
35-mm Dish No. 1.5 Coverslip 14-mm Glass Diameter Poly-D-Lysine Coated	MatTek Corporation	Cat#P35GC-1.5–14-C
300 Mesh Copper Grid with Formvar/Carbon Coating/Film	Electron Microscopy Sciences	Cat#FCF300-Cu

REAGENT or RESOURCE	SOURCE	IDENTIFIER
Goat Anti-Rabbit IgG 5-nm Gold Beads	BBI Solutions	Cat#EM.GAR5
OMIX C18 Pipette Tips	Agilent Technologies	Cat#A570033100
EasySpray C18 column (3-μm, 75 μm diameter × 150 mm length)	ThermoFisher Scientific	Cat#ES800A